THESIS

SPATIOTEMPORAL VARIATIONS IN LIQUID WATER CONTENT IN A SEASONAL SNOWPACK: IMPLICATIONS FOR RADAR REMOTE SENSING

Submitted by

Randall Ray Bonnell

Department of Geosciences

In partial fulfillment of the requirements

For the Degree of Master of Science

Colorado State University

Fort Collins, Colorado

Summer 2020

Master's Committee:

Advisor: Daniel McGrath

Steven Fassnacht
Kristen Rasmussen

ABSTRACT

SPATIOTEMPORAL VARIATION IN LIQUID WATER CONTENT IN A SEASONAL SNOWPACK: IMPLICATIONS FOR RADAR REMOTE SENSING

Mountain snowpacks act as seasonal reservoirs, providing a critical water resource to ~1.2 billion people globally. Regions with persistent snowpacks (e.g., mountain and polar environments) are responding quickly to climate change and are warming at faster rates than low-elevation temperate and equatorial regions. Since 1915, snow water equivalent (SWE) in the western U.S. snowpack has declined by 21% and snow covered area is contracting in the Rocky Mountains. Despite the clear importance of this resource and the identification of changes affecting it, no current remote sensing approach can accurately measure SWE at high spactiotemporal resolution. L-band (1-2 GHz) Interferometric Synthetic Aperture Radar (InSAR) is a promising approach for detecting changes in SWE at high spatiotemporal resolution in complex topography, but there are uncertainties regarding its performance, particularly when liquid water content (LWC) is present in the snowpack. LWC exhibits high spatial variability, causing spatially varying radar velocity that introduces significant uncertainty in SWE-retrievals. The objectives of this thesis include: (1) examine the importance of slope, aspect, canopy cover, and air temperature in the development of LWC in a continental seasonal snowpack using 1 GHz ground-penetrating radar (GPR), a proxy for L-band InSAR, and (2) quantify the uncertainty in L-band radar SWE-retreivals in wet-snow. This research was performed at Cameron Pass, a high elevation pass (3120 m) located in north-central Colorado, over the course of multiple survey dates during the melt season of 2019. Transects were chosen which represent a range in slope,

aspect and canopy cover. Slope and aspect were simplified using the northness index (NI). Canopy cover was quantified using the leaf area index (LAI). Positive degree days (PDD) was used to represent available melt-energy from air temperature.

The spatiotemporal development of LWC was studied along the transects using GPR, probed depths, and snowpit measured density. A subset of this project substituted Terrestrial LiDAR Scans (TLS) for probed depths. Surveys (17 in total, up to 3 surveys per date) were performed on seven dates which began on5 April 2019, where LWC values were ~0 vol. %, and ended on 19 June 2019 where LWC values exceeded 10 vol. %. Point measurements of LWC were observed to change (ΔLWC) by +9 vol. % or -8 vol. % over the course of a single day, but median ΔLWC were ~0 vol. % or slightly negative. LAI was negatively correlated with LWC for 13 out of the 17 surveys. NI was negatively correlated with LWC for 10 out of the 17 surveys. Multi-variable linear regressions to estimate ΔLWC identified several statistically significant variables (p-value < 0.10): LAI, NI, ΔPDD, and NI x ΔPDD. Snow-on Terrestrial LiDAR Scans (TLS) were conducted twice during the melt season, and a snow-off scan was conducted in late summer. Snow-on scans were differenced from the snow-off scan to produce distributed snow depth maps. TLS-derived snow depths compared poorly with probe-derived depths, which is attributed to poor LiDAR penetration through the thick vegetation present during the snow-off scan.

Finally, radar measurements of SWE (SWE-retrievals), if coupled with velocities derived from dry-snow densities, overestimated the mean SWE along transects by as much as 40% during the melt season, highlighting a potential issue for water managers during the melt season. Future work to support the testing of L-band radar SWE-retrievals in wet-snow should test radar signal-power attenuation methods and the capabilities of snow models for estimating LWC.

ACKNOWLEDGEMENTS

The research presented herein was funded by NASA Terrestrial Hydrology Program Award 80NSSC18K0877 (PI Dr. Daniel McGrath). Dr. McGrath, thank you for selecting me as a student for this project - I've learned so much from you and I am grateful for the many opportunities that came with this project. The countless hours of feedback and direction you tirelessly gave throughout my M.S. program have made me a better scientist. To my other committee members, Dr. Steven Fassnacht and Dr. Kristen Rasmussen, thank you for your flexibility and invaluable feedback. I am excited for any future collaborations we may have. I was taught Snow Hydrology by Dr. Steven Fassnacht, who also showed me how to dig snowpits and make extensive observations. To Dr. Ryan Webb, of the University of New Mexico, thank you for your willingness to converse and answer my questions regarding liquid water content and ground-penetrating radar.

More than 70 snowpits were dug to support this research! Thank you Alex Olsen-Mikitowicz, Bri Rick, Rosie Duncan, Tyler Miller, Will Gnesda, and the Snow Hydrology Field Methods Class for your exceptional field work! I'm so grateful that I didn't have to dig those pits by myself and you helped to make the research fun and enjoyable.

To my fellow CryoCrew Researchers, Bri Rick and Lucas Zeller, thank you for the laughs and your support. It's been a pleasure working with you. To the many other CSU Geosciences faculty and graduate students, thank you for your kindness and your support. I learned so much from my coursework and collaborations.

Finally, I could not have completed this program without the love and support of my family and friends. Grace, my wife, you are amazing and my love for you continues to grow.

Thank you for your never-ending patience and for being willing to move across the country to pursue a new life. To my mom and dad, thank you for always believing in me. Your support has been a cornerstone in my life.

TABLE OF CONTENTS

LIST OF TABLES

LIST OF FIGURES

1. Introduction

1.1 Seasonal Snow as a Water Resource

Snow is an essential component of Earth's hydrologic, biologic, and climate systems (Warren 1982; Doesken and Judson, 1996; Barnett et al., 2005; Keller et al., 2005; Niittynen et al., 2018). Snow is highly reflective, with an albedo between 50 and 90% in the visible spectrum (Warren, 1982) and covers up to 63% of the land mass in the Northern Hemisphere (Hammond et al., 2018; Kim 2018), and thus has a strong influence on Earth's climate system. In mountain regions, cooler temperatures and orographic lift lead to the deposition of snowpacks (Varhola et al., 2010; Snauffer et al., 2016) that act as seasonal reservoirs, providing a critical water resource to ~1.2 billion people globally (Barnett et al., 2005). In the western U.S., snow melt contributes 70-80% of the total annual runoff (Doesken and Judson, 1996; Clow, 2010), supporting agriculture, hydroelectric production, and recreational activities. Snow cover and snow melt support unique habitats (Keller et al., 2005) that contribute to global biodiversity (Niittynen et al., 2018). Grievously, regions with persistent snowpack (e.g., mountain and polar regions) are responding quickly to climate change and are warming at faster rates than low-elevation temperate and equatorial regions (Pepin et al., 2015; Huang et al., 2017).

During the last century, warming temperatures have driven a 21% decline in snow water equivalent (SWE; Mote et al., 2018) and reduced the extent and duration of snow cover in the western U.S. (Dettinger et al., 2004; Stewart et al., 2005; Hall et al., 2015). While a complete analysis for changes in snow covered area has yet to be published, two case studies stand out. In Colorado, the melt season is initiating earlier by 4.8 days decade^{-1} since 1978 (Clow, 2010). In the Wind River Range, WY, snow cover depletion rates have been increasing since 1972 and

complete melt-out occurs 25 days earlier (Hall et al., 2015). Additionally, warming temperatures are projected to change the dominant precipitation phase that falls during traditionally snow-dominated months and drive the rain-snow transition zone upward in elevation (Klos et al., 2014). Collectively, these changes indicate a shift in the historic baseline and suggest a completely new paradigm for mountain snowpacks by the end of the century.

Globally, much remains to be understood about mountain snowpacks, particularly in the face of shifting baselines across the U.S. and the world. SWE, the mass of snow per unit area, is an essential and defining variable of the snowpack, but its spatial variability is not easily measured. SWE is used for forecasting runoff, managing water resources, and predicting drought conditions. In particular, drought forecasting is projected to become more difficult as the western U.S. experiences a decline in snowfall and a higher dependence on rainfall (Livneh and Badger, 2020). Despite the clear importance of this resource and the identification of changes affecting it, there are major limitiations in measuring SWE at regional and global scales, which hinder the management of this critical resource.

1.2 Remote Sensing Methods for Snow Water Equivalent

Numerous approaches are utilized to estimate or measure SWE, but each approach suffers from limitations and uncertainties. Physically based models run at the regional level (e.g., SNODAS) produce SWE estimates at coarse resolution (1 km) and have greater uncertainty at elevations above tree-line due to a lack of in-situ observations (i.e., SNOTEL stations; Dozier et al., 2016). Passive microwave (PM) sensors, one of the original tools for the remote sensing of SWE, are limited to measuring SWE in shallow (< 200 mm) snowpacks (Takala et al., 2011; Dozier et al., 2016) and have increased uncertainty in complex topography, due, in part, to the coarse spatial footprint of PM sensors (Mote et al., 2003; Shi et al., 2016). Light detection and

ranging (LiDAR) instruments are capable of resolving fine-scale (< 1 m) snow depth heterogeneity, but require a density model to determine SWE at regional scales and are largely limited to airborne platforms, which becomes cost-prohibitive at regional scales (Painter et al., 2016; McGrath et al., 2019). Recent developments in photogrammetry have established methods to map snow depths through high resolution commercial satellite stereo imagery (Shean et al., 2016), but this method is most suited to environments free of tree-cover (McGrath et al., 2019) and also requires a density model to estimate SWE. L-band radar is sensitive to SWE changes and L-band Interferometric Synthetic Aperture Radar (InSAR) is a promising instrument for estimating changes in SWE at high resolutions in complex topography (Deeb et al., 2011). Unfortunately, this approach is relatively untested and there are uncertainties regarding its performance in various environments, especially wet-snow.

A principal model used by U.S. water managers is the Snow Data Assimilation System (SNODAS), operated by the National Snow and Ice Data Center (NSIDC). SNODAS provides daily SWE estimates at 1 km resolution, utilizing 100,000 meteorological stations, 40,000 in-situ observation sites for snow, and snow-covered area satellite products (Dozier et al., 2016). In the U.S., the Natural Resources Conservation Service manages >800 Snow Telemetry (SNOTEL) stations, which monitor mountain environments across 13 different states and British Columbia, Canada (Snow Survey and Water Supply Forecasting Program, Accessed 22 June 2020). SNOTEL stations include snow pillows, a sub-snow, non-destructive tool for measuring SWE (Serreze et al., 1999). Unfortunately, SNOTEL stations are expensive to deploy and maintain (~$25,000 to install) and act as a point observation (Fassnacht and Hultstrand, 2015), thus limiting their ability to capture the true surounding SWE heterogeneity (Meromy et al., 2013). Snow pillow distribution is largely limited to regions with persisting snowpacks (Daly et al.,

2000) and below tree-line to avoid wind exposure and higher avalanche risk. SNODAS 1 km SWE products are difficult to interpret in topographically complex regions and have been shown to misrepresent snow distribution at higher elevations due to the absence of snow pillows above tree-line (Dressler et al., 2006; Dozier et al., 2016). Reanalysis products, similar to physical models, utilize current and historical data from thousands of in-situ data stations with climatological forcings to predict SWE distribution across large regions (Snauffer et al., 2016). Reanalysis products have been found to underestimate SWE (Broxton et al., 2016), but recent efforts offer improvements for SWE estimation (Wrzesien et al., 2020).

Snow is largely transmissible in the microwave spectrum and PM is one of the original remote sensing methods for snow, with studies beginning in the 1970s (e.g., Chang et al., 1976; Foster et al., 1980). SWE calculations rely on the extinction difference between PM bandwidths (Dozier et al., 2016; Shi et al., 2016). Due to its high repeat-orbital path, PM has proven a valuable tool for measuring SWE in regions where SWE and terrain are relatively homogenous and where SWE is less than 150-200 mm, such as the Canadian Prairies (Goodison and Walker, 1993; Mote et al., 2003; Dozier et al., 2016). As SWE increases beyond 150-200 mm, it becomes a microwave emission source, yielding indiscernible extinction differences between different PM bands (Takala et al., 2011). PM measurements have very coarse resolution (~25 km; Dozier et al., 2016), and therefore cannot accurately characterize the spatial heterogeneity inherent to mountain snowpacks in complex topography, however, new methods have used interpolation methods to increase the spatial resolution to 3.125 km (Brodzik et al., 2018). PM has the unique ability in distinguishing between wet and dry snow, but is unable to measure SWE in wet-snow conditions (Mote et al., 2003; Dozier et al., 2016).

Airborne LiDAR is an effective tool for accurately measuring snow depth at < 1 m horizontal resolution (Hopkinson et al., 2004; Deems et al., 2013; Painter et al., 2016). Perhaps the most well-known example, LiDAR was employed on NASA's Airborne Snow Observatory (ASO) for surveys in the Sierra Nevada during the severe 2011-2017 California Drought, dramatically improving estimates of SWE (as compared to point observations from SNOTEL stations) for water managers (Henn et al., 2018). To measure snow depth, LiDAR snow-off scans are differenced from snow-on scans of the same location (Deems et al., 2013; Painter et al., 2016; McGrath et al., 2019). LiDAR does not measure SWE directly, instead, a snow density model is used to calculate SWE from snow depth (Painter et al., 2016). Density is assumed to vary much less than SWE, which is correlated with snow depth variability (Logan 1973; Elder et al., 1991; Lopez-Moreno et al., 2013). Airborne LiDAR is well-suited to small regions, but would be cost-prohibitive to implement on regional to global scales. Satellite-borne LiDAR systems, including NASA's ICESat and ICESat-2, provide global coverage, but rarely have repeated orbital tracks in the mid-latitudes and have much larger footprints than airborne LiDAR. Still, ICESat data has been used to estimate snow thickness on Arctic sea ice (Kwok and Cunningham, 2008) and NASA SnowEx is testing ICESat-2's capability for measuring snow depth in the western U.S.

InSAR has been used to map snow cover (Tsai et al., 2019), snow depth from airborne Ka-band (Moller et al., 2017), and most recently, snow depth at 1 km resolution in non-forested regions from Sentinel-1 C-band cross-polarization and co-polarization backscatter ratios (Lievens et al., 2019). A promising approach for remotely measuring SWE is the use of L-band (1-2 GHz) radar interferometry (Deeb et al., 2011). The longer wavelength of L-band radar (15-30 cm in a vacuum) enables high transmissivity and a penetration depth (defined as the distance

travelled at which the signal power is 1/*e* of the original transmitted signal) in dry-snow of up to 400 m (Koch et al., 2014; Tsai et al., 2019) and the high contrast between ground and snow dielectric permittivities enables easy identification of the ground surface (Manickam and Barris, 2020). L-band InSAR remains largely untested in snow: the first major test was flown as part of the SnowEx 2017 Grand Mesa, CO Campaign, but minimal changes in SWE between flights prevented a thorough assessment (Marshall et al., 2019; Manickam and Barros, 2020). NASA's UAVSAR, a L-band InSAR sensor, collected observations as part of the SnowEx 2020 Time Series Campaign and Grand Mesa Intensive Operation Period. A NASA-ISRO L-band InSAR satellite mission (NISAR) is scheduled for launch in 2022, with 100 m spatial resolution and ~12 day repeat ground coverage. High repeat ground coverage is especially important to maintain coherence between scans. However, NISAR does not have Level-1 science requirements specific to snow, so further evaluation of this approach is a high priority.

One such effort to evaluate this approach occurred during the NASA SnowEx 2020 Time Series campaign, which included weekly to bi-weekly repeat observations at 13 mountain sites across the western U.S. The NASA SnowEx project is a multi-year campaign designed to develop an optimal space-borne approach for measuring SWE by testing several remote sensing instruments. This campaign represents the most comprehensive assessment of L-band InSAR for SWE-retrieval, nonetheless, it is expected that significant uncertainties will remain in wet-snow conditions and forested areas.

1.3 Ground-penetrating Radar Applications in Snow

This research uses surface-coupled L-band ground-penetrating radar (GPR), but the findings have implications for airborne and satellite-borne L-band InSAR. The radar physics in snow is similar between GPR and InSAR, although some key differences exist between the

specific methods. GPR produces geolocated radar profiles, referred to as radargrams, while InSAR is a change detection approach, requiring repeated overpasses to map changes in travel-time that occur from one flight to the next (Deeb et al., 2011). Unlike InSAR, GPR is a well-validated methodology form measuring SWE (e.g., Koh et al., 1996; Marshall and Koh, 2008), making it an ideal instrument to evaluate L-band InSAR capabilities.

GPR applications in snow remote sensing include measuring snow depth/SWE and measuring snow permittivity, which allows the estimation of snow density in dry-snow or the estimation of LWC in wet-snow when density is known. The most common method is to use GPR to measure spatially extensive and continuous snow depth and/or SWE. In dry-snow, radar velocity is sensitive to snow density (Lundberg et al., 2005) and GPR has accurately measured snow depths in maritime and continental snow climates (McGrath et al., 2018; McGrath et al., 2019). In wet-snow, radar is sensitive to both density and LWC. Several developments in GPR methodology have dramatically increased the understanding of LWC (e.g., Bradford et al., 2009; Schmid et al., 2014; Webb et al., 2018a).

1.4 Liquid Water Content

LWC development controls snow melt runoff, which is vital information for water managers in predicting runoff (Techel and Pielmeier 2011; Schmid et al., 2014). LWC is introduced into the snowpack through surface melt or through rain-on-snow, as both air temperature (hence long-wave radiation) and short-wave radiation increase in the spring (Fierz et al., 2009). Rain-on-snow events are currently rare in continental climates in mid-winter and are more common in maritime climates (McCabe et al., 2007). LWC at the snow surface reduces albedo (Warren 1982), thereby increasing absorbed short-wave radiation. LWC penetration and refreezing is a primary contributor to snowpack ripening. These positive feedbacks lead to the

release of melt water into drainage areas and the subsurface. LWC can be calculated in a snowpit using calorimetry methods, by melting snow in water (Kawashima et al., 1998). This method is time consuming (~2 min per measurement) and more efficient methods have been developed that utilize dielectric permittivity measurements taken by capacitive sensors. Two prominent dielectric methods include the Denoth meter (Denoth, 1994), which utilizes a large plate inserted into the snowpit face, and the Finish Snow Fork (Sihvola and Tiuri, 1986), which utilizes a two-prong fork inserted into the snowpit face. Both methods use empirically derived formulas, utilizing density and bulk permittivity and are two of the three prominent dielectric LWC equations. The third equation, derived from Roth et al. (1990), utilizes a three-phase mixing formula, with the permittivities and densities of ice, water, and air. Although these equations agree reasonably at lower permittivities, as permittivity increases, the three equations disagree substantially (Koch et al., 2014, Webb et al., 2018a), indicating a poor understanding of the permittivity-LWC relation and a need for a better empirical or physically based equation.

Previous studies of LWC show a strong seasonal and diurnal relation between LWC and air temperatures (Koch et al., 2014; Schmid et al., 2014; Heilig et al., 2015). LWC values exceeding 4 vol. % are linked to melt output (Schmid et al., 2015). LWC values are shown to vary spatially by as much as 19 vol. % between neighboring pixels at 3 m resolution (Webb et al., 2018a). LWC development is linked to slope, aspect, and canopy cover (DeWalle and Rango, 2008). LWC is carried through the snow by percolation through pore spaces or by flow through developed flowpaths (Techel and Pielmeier, 2011), which are observed both within the snowpack and at the ground-snow interface. At the ground-snow interface, preferential flowpaths develop along hillslopes, causing water to pool where a hillslope transitions to flatter slopes (Webb et al., 2018b). As slope increases, the capabilities of intra-snowpack flowpaths to move

melt-water also increases (Webb et al., 2020). Flowpath development may also be linked to aspect, where one study found more extensive development of flowpaths at the ground-snow interface on a north-facing hillslope than one with south aspect (Webb et al., 2018b). The relation between LWC and forests has not been well established. Forests act as a long-wave irradiance input, but attenuate short-wave radiation due to shading (Sicart and Essery, 2004). At high canopy densities, the long-wave input is roughly equivalent to the short-wave attenuation.

1.5 Study Objectives

This thesis has two primary objectives: (1) examine the importance of terrain, canopy cover, and air temperature in the development of LWC in a continental seasonal snowpack using 1 GHz GPR and (2) quantify the uncertainty in L-band radar SWE retreivals due to the presence of LWC. A thorough uncertainty analysis provides insight to the expected accuracy of L-band InSAR measurements from current SWE-retrieval algorithms during the melt season. The relations between LWC spatiotemporal variability, terrain parameters, and air temperature will provide a basis for future work to develop more accurate SWE-retrieval algorithms in radar applications.

2. Ground-penetrating Radar Theory

2.1 L-band Ground-penetrating Radar

L-band (1-2 GHz; 15-30 cm wavelength in a vacuum) radar is highly transmissible through snow due to its long wavelength (10-20 cm wavelength in snow) relative to snow grain size. At higher frequencies/shorter wavelengths, radar penetration into snow decreases: C-band (4-8 GHz; 3.75-7.5 cm wavelength in a vacuum) radar signal scatters with larger snow crystals (Shi and Dozier, 2000), while Ka-band (26.5-40 GHz; 0.75-1.11 cm wavelength in a vacuum) simply reflects off the snow surface (Moller et al., 2017). Radar systems record travel-time between signal transmission and return, i.e. two-way travel-time (*twt*), and plots the amplitude value of each signal return as a radargram. The vertical resolution for radar systems is estimated at $1/4^{th}$ the wavelength, or 2.5-5 cm for L-band radar in snow (Blindow 2006). Radar wave propagation is controlled by a media's dielectric permittivity. The high contrast between ground and snow dielectric permittivities enables easy identification of the ground surface (Gubler and Weilenmann, 1986; Koh et al., 1996; Marshall and Koh, 2008; McGrath et al., 2019). In snow, radar velocity (v_s) is a function the real component of snow permittivity (ε_s; Equation 2.1). The real component of permittivity is described in Equation 2.2 by a three-phase mixing formula (Roth et al., 1990): ε_{eff} is a function of bulk dry-snow density ($\rho_{s\text{-}d}$), % volumetric liquid water content (LWC), and the known permittivities of ice (ε_i), water (ε_w), and air (ε_a). Permittivity increases with snow density, resulting in a slower radar velocity (Figure 2.1a). Permittivity significantly increases with increasing LWC, further perturbing radar velocity (Figure 2.1b). Radargram interpretation is relatively straightforward in dry-snow (Deeb et al., 2011). Velocity

is estimated from bulk snow density, *twt* is converted to snow depth (d_s, Equation 2.3), and SWE is calculated using Equation 2.4.

$$v_s = \frac{c}{\sqrt{\varepsilon_s}} \quad \text{(Equation 2.1)}$$

$$\varepsilon_s = \left(0.01 * LWC * \sqrt{\varepsilon_w} + \frac{\rho_{s\text{-}d}}{\rho_i} * \sqrt{\varepsilon_i} + \left(1 - \frac{\rho_{s\text{-}d}}{\rho_i} - 0.01 * LWC\right) * \sqrt{\varepsilon_a}\right)^2 \quad \text{(Equation 2.2)}$$

$$d_s = v_s * \frac{twt}{2} \quad \text{(Equation 2.3)}$$

$$SWE = d_s * \rho_{s-d} \quad \text{(Equation 2.4)}$$

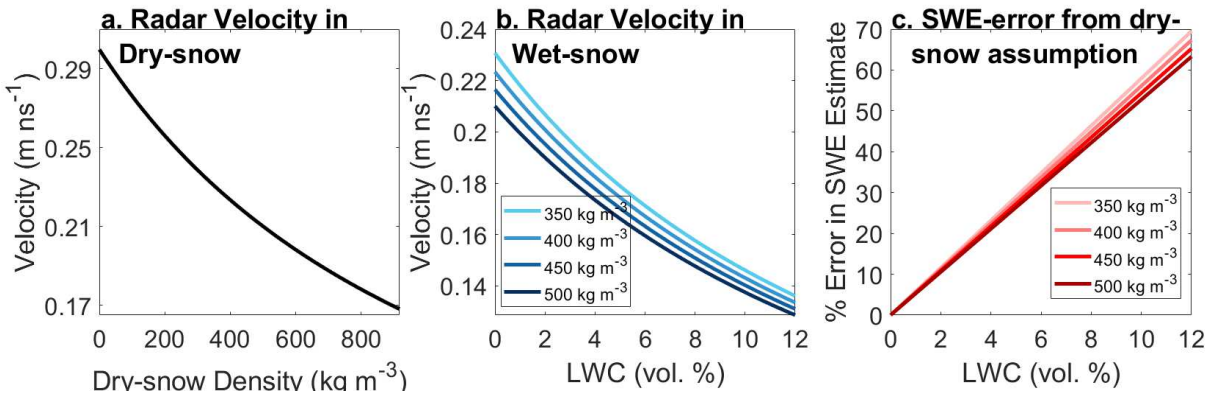

Figure 2.1: (a.) Radar velocity as a function of dry-snow density. (b.) Radar velocity as a function of LWC and density. (c.) SWE-error calculated as the percent difference between radar velocities that account for LWC and radar velocities that do not. Figure uses Equation 2.2 to relate permittivity, density, and LWC.

2.2 Wet-snow Uncertainties

Snow is a multi-phase system. Dry-snow, a mixture of air and ice, has a permittivity that can be described with one real component. Wet-snow, a mixture of water, air, and ice, has a complex permittivity described with a real component and an imaginary component. Roth et al. (1990) describes the real component of permittivity through a three-phase mixing formula (Equation 2.2). Sihvola and Tiurri, (1986) empirically derived a relation between LWC, dry-

snow density, and the real component of permittivity (Equation 2.5). Denoth (1994) derived a different empirical equation using LWC, wet-snow density (Equation 2.7), and the real component of permittivity (Equation 2.6). These equations describe the relation between LWC and the real component of permittivity differently, with disagreement growing as LWC increases (Koch et al., 2014).

$$\varepsilon_s = 1 + 0.0017 * \rho_{s\text{-}d} + 7.0 * 10^{-7} * \rho_{ds}^2 + 0.087 * LWC + 0.007 * LWC^2$$

(Equation 2.5)

$$\varepsilon_s = 1 + 0.00192 * \rho_s + 4.4 * 10^{-7}{\rho_s}^2 + 0.187 * LWC + 0.0045 * LWC^2$$

(Equation 2.6)

$$\rho_s = \rho_{s-d} + 0.01 * LWC * \rho_w \quad \text{(Equation 2.7)}$$

Interpreting L-band radargrams in wet-snow (when snowpack pore spaces contain LWC) is more difficult due to uncertainties in radar-derived SWE arising from frequency-dependent signal attenuation and velocity variability (Bradford 2009; Schmid et al., 2015; Webb et al., 2018a). Unlike snow density, LWC is not measured remotely at snow observation stations (e.g., SNOTEL stations) and the timing of its development is difficult to predict. LWC development in the snowpack depends on the net (short-wave and long-wave) energy balance, topographic variables, canopy cover, and any preceding days of melt (Techel and Pielmeier, 2011). Radar velocity is inversely related to permittivity: increased LWC causes decreased radar velocity (Figure 2.1b). The spatial diversity of topographic variables and vegetation drive the heterogeneous development of LWC, thereby creating spatially distinct permittivity which makes radar velocity difficult to generalize (Webb et al., 2018a). Without any knowledge of the progression of LWC development, a radargram which uses a local SNOTEL station density

measurement for SWE calculation in the melt season, can overestimate SWE by as much as 70% for 12 vol. % LWC (Figure 2.1c). Thus, radar SWE-retrievals carry significant uncertainties during the melt season.

2.3 Estimating LWC from Radargrams and Snow Depths

LWC is directly measured with radar by using coincident snow depths and *twt* to constrain velocity (Equation 2.8) and calculte snow permittivity (Equation 2.1). Then, using a

$$v_s = 2 * \frac{d_s}{twt} \quad \text{(Equation 2.8)}$$

measured snow density or estimated dry-snow density, Equations 2.2, 2.5, and 2.6 can be used to calculate LWC. This technique is fairly new. Schmid et al. (2014, 2015) continuously derived LWC for a full melt season by combining an upward looking stationary GPR system below the snow to measure *twt*, a snow stake mounted near the GPR system to measure snow depth, and a snow pillow to measure density. They showed a correlation between time-of-day and LWC and linked bulk LWC values > 4.0 vol. % to increases in melt-water output. Webb et al. (2018a) used surface-coupled GPR mounted on a sled to measure the spatial variability of LWC, and found that LWC exhibits high spatial variability, with LWC varying as much as 19.5 vol. % between neighboring 3 m pixels.

3. Study Site and Methods

3.1 Study Site

Cameron Pass is a high elevation pass (3120 m) located between the Medicine Bow and Never Summer Ranges of north-central Colorado and is an important headwaters region for the Cache la Poudre River Basin. The region is forested with Engleman spruce (*Picea engelmanii*), subalpine fir (*Abies lasiocarpa*), lodgepole pine (*Pinus contorta*), and Aspen (*Populus tremuloides*), with interspersed meadows (Figure 3.1a; Fassnacht et al., 2018). Three transects were chosen, each representing a unique set of of terrain parameters and canopy densities. The North Transect has an elevation range of 3120-3126 m, 0-5° slopes, NE aspect, and 20-70% canopy cover. The Meadow Transect has an elevation range of 3121-3126 m, flat aspect and no canopy cover, but is shaded until mid-morning (~09:00 MDT for June) by the north ridge of Iron Mountain (3670 m). The South Transect has an elevation range of 3111-3123 m, 3-14° slopes, W-S aspect, and canopy that varies from no cover in the southernmost portion of the transect to ~70% in the western portion of the transect.

3.2 Terrain and Canopy Variables

The three transects were further characterized using the Northness Index (NI; Molotch et al., 2005) and the Leaf Area Index (LAI). NI (Equation 3.1; Figure 3.1b) was calculated along each transect using the 10 m resolution National Elevation Dataset (Equation 3.2; Gesch et al., 2002). NI, which is a function of aspect and slope, encapsulates differences in exposure to

$$NI = \cos(aspect) * \sin(slope) \quad \text{(Equation 3.1)}$$

solar radiation, where values close to −1 have high exposure and values close to 1 have low exposure. In addition, LAI (Equation 3.2; Saito et al., 2001) was calculated aong each transect using a Normalized Difference Vegetation Index (NDVI) from Sentinel-2 Level 2A imagery obtained during snow cover on 29 March 2019 (Figure 3.1c). LAI is a quantitative assessment of the leaf-covered area within a pixel.

$$LAI = 0.57 * 2.72^{2.33*NDVI} \quad \text{(Equation 3.2)}$$

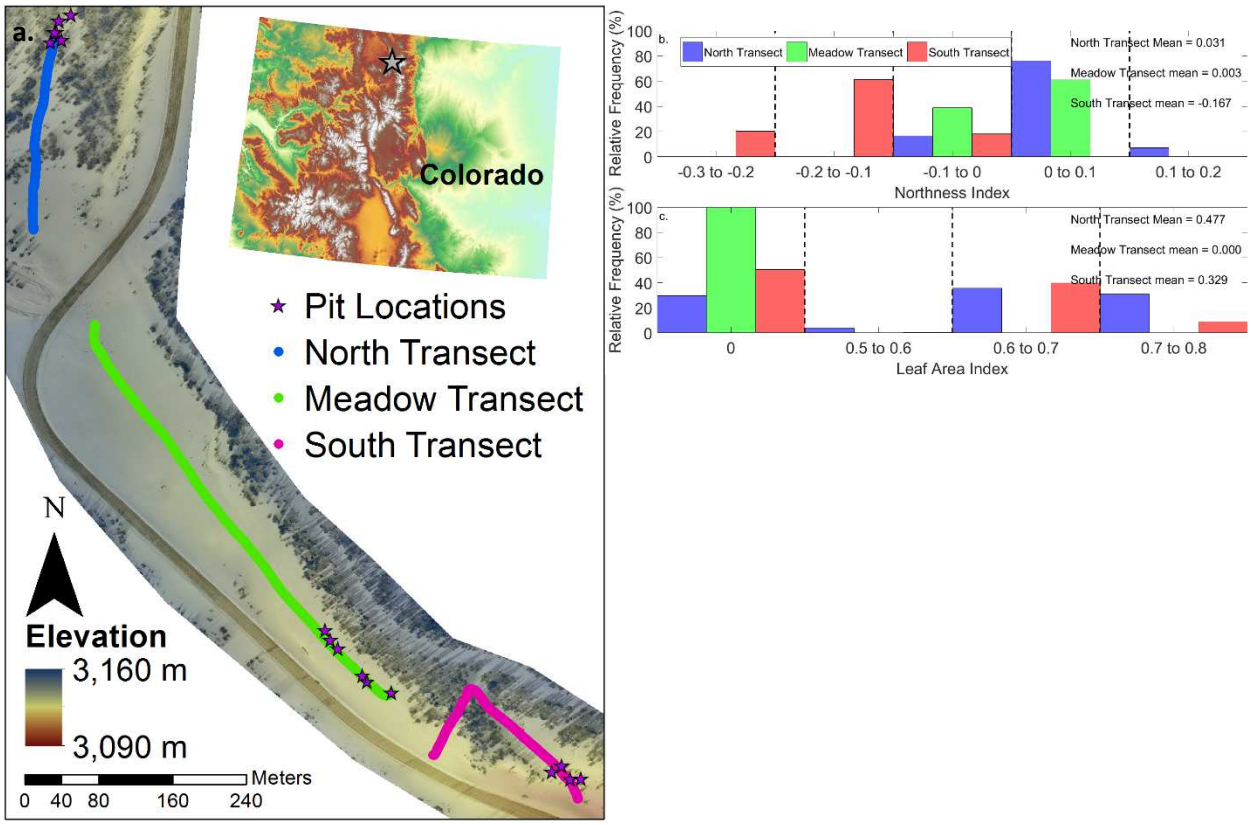

Figure 3.1: (a.) Three transects are outlined with snowpit locations. Location for Cameron Pass is shown in inset. (b.) NI distribution and (c.) LAI distribution along the three transects. Orthomosaic and DEM in (a.) derived from drone survey in March 2020. DEM in inset obtained from the Shuttle Radar Topography Mission.

3.3 Nearby Automated Stations

The Joe Wright SNOTEL station (Site Number: 551) is located 1.4 km to the northeast of our study site at 3084 m elevation and provides automated hourly measurements of SWE, snow

depth, and air temperature. With LAI = 0.739 and NI = 0.096, Joe Wright SNOTEL station represents an area that is most similar to the North Transect. Joe Wright SNOTEL station has recorded air temperature and SWE since 1978 and snow depth since 2005, providing a long-term climatological perspective (Ma et al., 2019). This assessment used the 2009-2018 daily records of SWE and average temperature to calculate median values for April-June SWE, temperature, and length of melt season (Equation 3.3) for comparison with 2019 daily records. Additionally, 2019 hourly snow depth and air temperature records were used in this study to calculate hourly snow depth loss and model available melt energy, respectively.

$$Melt\ Season\ Duration = Peak\ SWE\ Date - Snow\ Off\ Date \quad \text{(Equation 3.3)}$$

Two automated stream gages were used for this analysis: USGS stream gage #06746095 and Colorado Division of Water Resources stream gage MICDCPCO. Stream gage MICDCPCO is located within the field site and measures discharge from the regulated Michigan Ditch, which diverts water from the Michigan River to Joe Wright Creek. Stream gage #06746095 is ~2.4 km to the northeast of the field site and measures discharge on the Joe Wright Creek below its confluence with the Michigan Ditch. Michigan Ditch discharge was subtracted from Joe Wright Creek discharge to remove the regulated water input effects. Discharge was normalized to basin area (8.13 km^2) and compared to SNOTEL SWE-loss.

3.4 Observational Period

The Joe Wright SNOTEL station 2009-2018 median peak SWE occurs on 5 May (with a standard deviation of ±27 days) and the median snow off date is 17 June (with a standard deviation of ±13 days). Field surveys were scheduled to capture LWC variability throughout the melt season, consisting of a pre-melt dry-snow survey (5 April survey), an initial melt season

survey (25 April survey), and middle to late season surveys (17 May, 3 June, 4 June, 10 June, and 19 June). Survey dates are outlined in Table 3.1.

3.5 Field Methods

3.5.1 In-situ Measurements

For each survey date, at least one snowpit was dug and snow depth was sampled along the transects before pulling the GPR unit (described in Section 3.5.2). Snow depth measurements were acquired at 3 m intervals using a Snowmetrics depth probe and their locations were recorded using fiducials marked in the GPR control unit. Four standard observations were made in snowpits, (1) snow stratigraphy was identified, (2) snow density was measured at 10 cm intervals along two adjacent vertical columns using a 1000 cm^3 wedge cutter, (3) snow temperature was measured at 10 cm intervals along one vertical profile using a digital thermometer, and (4) % volumetric LWC was measured along two adjacent vertical columns using the SLF Snow Sensor (SLF Snow Sensor – User Manual, Accessed on 23 June 2020), a capacitive sensor that measures dielectric permittivity of the snow surface it contacts. For morning surveys (08:00-12:00 MDT), pit observations followed a specific workflow: (1) temperature and LWC were measured as soon as the snowpit face was cut, (2) stratigraphic units were measured and described, and (3) density measurements were sampled. For the Midday (12:00-16:00 MDT) and Evening (16:00-19:00 MDT) snowpit surveys, a fresh snowpit face was cut 1-2 m back from the previous snowpit face and LWC observations were measured. Snow depth transects and snowpits were performed as outlined in Table 3.1. Only morning surveys were conducted on 5 April and 17 May. On 5 April, LWC was not observed in the snowpit, and any subsequent surveys likely would have revealed little change in LWC. On 17 May, air temperature at Joe Wright SNOTEL station peaked at 2.8 °C at 12:00 MDT and fell as clouds

moved in and snow began precipitating, presumably limiting further LWC increases in the snowpack.

Table 3.1: Observations performed for each survey date. Depth transects were performed once per survey date, where C denotes a complete transect and P denotes a partial transect. GPR transects were performed up to three times per survey date.

	North Transect	Meadow Transect	South Transect
5-Apr	Depth transect - P GPR transect - 1	Depth transect - P Snowpit GPR transect - 1	Depth transect - P GPR transect - 1
25-Apr	Depth transect - P Snowpit GPR transect - 3	Depth transect - P Snowpit GPR transect - 3	Depth transect - P Snowpit GPR transect - 3
17-May	Depth transect - C Snowpit GPR transect - 1	Depth transect - P Snowpit GPR transect - 1	Depth transect - C Snowpit GPR transect - 1
3-Jun	Depth transect - C Snowpit GPR transect - 2	Depth transect - C Snowpit GPR transect - 3	Depth transect - C Snowpit GPR transect - 3
4-Jun	Depth transect - C Snowpit GPR transect - 3	Depth transect - C Snowpit GPR transect - 3	Depth transect - C Snowpit GPR transect - 3
10-Jun	Depth transect - C Snowpit GPR transect - 3	Depth transect - C Snowpit GPR transect - 3	Full melt out
19-Jun	Depth transect - C Snowpit GPR transect - 3	Full melt out	Full melt out

3.5.2 Ground-penetrating Radar Measurements

Common-offset GPR surveys were performed on each transect for Morning, Midday, and Evening surveys using a Sensors & Software GPR system and 1 GHz center-frequency antennas. Midday and Evening surveys were not performed for 5 April and 17 May. Additional GPR was collected in two spiral grids on 25 April and 3 June, coinciding with the supplementary TLS

scans for mapping snow depth. The GPR unit was mounted in the base of a plastic sled, thereby coupling the antennas to the snow surface, and was manually pulled at ~1 m s^{-1}. Traces were recorded every 0.1 s with a time-sampling interval of 100 ps. An Emlid RS+ RTK system was used for geolocating GPR traces. The rover unit was mounted to the GPR antennas to geolocate traces in the control unit and the base station unit was mounted on a tripod near the northern end of the Meadow Transect. The Emlid RS+ uses the GPS (L1 frequency), GLONASS, GALILEO, QZSS, and SBAS constellations (described in Section 3.8.1).

3.5.3 LiDAR Measurements

UNAVCO was contracted to collect snow-on TLS for 25 April and 3 June and a snow-off TLS for 29 August using a Reigl VZ-6000. The Reigl VZ-6000 has minimum and maximum ranges of 5 m and 6000 m, respectively. The Meadow and South Transects and surrounding areas were scanned from three different positions. Raw point clouds between the scan locations were first aligned using snowshoe and sled tracks within the scanned areas. Further alignment was required to match scans from different dates, and this was accomplished using static features in the study area (e.g., signs, road surface). Point clouds were exported in WGS 84 Ellipsoid (EPSG:4376).

3.6 Snowpit Data Processing

To determine bulk snow density, layer averaged density measurements were used to calculate a column averaged density. Outliers were defined as measurements within a layer that exceeded ±20 kg m^{-3} difference from the initial measurement. In cases where layers contained an outlier and a third measurement was available, the outlier was removed from the averaging. In

cases where multiple density measurements along a layer disagreed by greater than ±20 kg m^{-3}, the average of the three measurements was taken for the layer average.

The SLF Snow Sensor uses an empirically derived equation (Equation 3.5) to calculate LWC from an input dry-snow density ($\rho_{s\text{-}d}$, Equation 3.4) and measured permittivity. Here, ρ_s is the measured snow density, ρ_w is the density of water at 0° C, ε_s is the snow permittivity measured by the SLF, and ε_{ds} is the theoretical dry-snow permittivity calculated from Equation 3.6 using the input dry-snow density estimate. A three-phase mixing formula (Equation 3.6) following Roth et al. (1990) was used to calculate the equivalent dry-snow permittivity, then, permittivity values were back-calculated for SLF measurements using a root-solving algorithm on Equation 3.5. Equation 3.6 uses LWC (assumed to be 0% for dry-snow), permittivity of water (ε_w), permittivity of ice (ε_i), permittivity of air (ε_a), and the density of ice (ρ_i). To recalculate SLF LWC measurements, Equation 3.4 was substituted into Equation 3.6 and solved for LWC (Equation 3.7). The most representative LWC measurements were chosen within layers, producing a single column of LWC measurements which were then averaged to calculate bulk LWC for each pit.

$$\rho_{s\text{-}d} = \rho_s - LWC * \rho_w \quad \text{(Equation 3.4)}$$

$$LWC = 0.271 * (\varepsilon_s - \varepsilon_{ds})^3 - 2.688 * (\varepsilon_s - \varepsilon_{ds})^2 + 10.337 * (\varepsilon_s - \varepsilon_{ds}) \quad \text{(Equation 3.5)}$$

$$\varepsilon_s = \left(0.01 * LWC * \sqrt{\varepsilon_w} + \frac{\rho_{s\text{-}d}}{\rho_i} * \sqrt{\varepsilon_i} + \left(1 - \frac{\rho_{s\text{-}d}}{\rho_i} - 0.01 * LWC\right) * \sqrt{\varepsilon_a}\right)^2 \quad \text{(Equation 3.6)}$$

$$LWC = \frac{\sqrt{\varepsilon_s} - \frac{\rho_s}{\rho_i} * \left(\sqrt{\varepsilon_i} - \sqrt{\varepsilon_a}\right) - \sqrt{\varepsilon_a}}{\sqrt{\varepsilon_w} - \frac{\rho_w}{\rho_i} * \left(\sqrt{\varepsilon_i} + \sqrt{\varepsilon_a}\right) - \sqrt{\varepsilon_a}} \quad \text{(Equation 3.7)}$$

3.7 Radargram Processing

3.7.1 Post-processing Trace Coordinates

For each survey date, the Emlid RS+ (Reach RS+ – RTK GPS receiver for high precision surveying, Accessed 23 June 2020) Base station was set to run for a minimum of 6 hours in order to correct GPR trace coordinates produced by the Emlid RS+ Rover unit. The Rover log was recorded in two places: the GPR unit recorded the Rover log and the Rover recorded its log internally. Post-processed Kinematics (PPK) was performed using the Emlid Reach RS+ RTK Library. For each survey date, the average position for the Base station was used to correct the Rover position file, providing <0.5 m positioning accuracy. Then, the GPR position file was corrected with the revised Rover position file on the basis of GPS time stamps.

3.7.2 Time-varying Time-zero Correction

For surface-coupled GPR units, time-zero is the exact time at which the radar wave is projected into the subsurface. Time-zero is not constant and varies with any changes in a material's characteristics, in addition to cable coupling and temperature variations (Rial et al., 2009). In shallow mediums, such as the Cameron Pass snowpack, not choosing the correct time-zero can introduce significant uncertainty in the measured two-way travel time (*twt*). To produce time-varying time-zero corrections, a custom Matlab script calculated time-zero by identifying the first positive peak (representing the time-zero) for every 10th radar trace.

3.7.3 ReflexW Workflow

Radargrams were processed using Sandmeier ReflexW software (Sandmeier, 2019). For each radargram, we applied the previously described time-varying time-zero correction, a dewow filter, a subtracting average filter, and an equidistant trace interpolation. The dewow filter is a 1-D filter applied to each trace to remove the DC-shift and improve the clarity of the radargram.

The subtracting average filter is a 2-D filter that takes the average of each sample along a given set of traces and subtracts it from the set of traces, essentially reducing instrument noise. Equidistant trace interpolation is a trace resampling and interpolation method that produces traces with equal spacing along the survey line, removing potential bias due to changes in sled velocity. Since this is a surface-coupled GPR system, the air-snow interface does not need to be identified. The ground-snow interface was identified for each radargram as a high-amplitude semi-continuous reflector and is most commonly the highest-amplitude (brightest) reflector at depth. The positive peak for the ground identification was manually picked to avoid introducing systematic bias from the time-zero correction. Picked *twt* was exported in ASCII format and adjusted for underlying topographic slope using the National Elevation Dataset 10 m DEM in Matlab (Equation 3.8). Here, twt_{meas} is the *twt* measured by the GPR and twt_{cor} is the corrected *twt* based on the underlying topographic slope. This topographic correction assumes a snow surface that mimics the underlying topography. An example of a fully processed radargram and picked line is provided in Figure 3.2.

$$twt_{cor} = \frac{twt_{meas}}{\cos(slope)} \qquad \text{Equation 3.8}$$

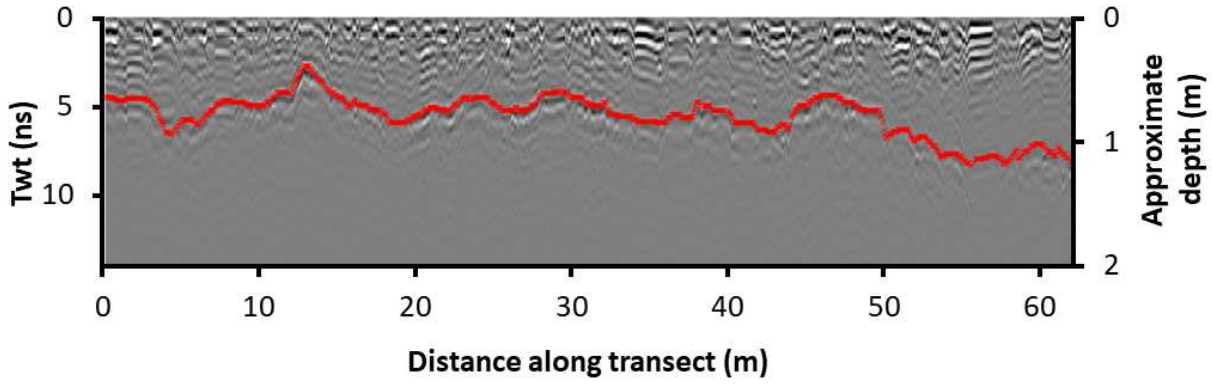

Figure 3.2: Processed radargram from the midday North Transect survey on 19 June 2019. The red line represents the picked ground-snow interface. Snow depth calculated using a radar velocity of 0.14 m ns^{-1}.

3.8 TLS Processing

3.8.1 Distributed Snow Depth Maps

Date-specific TLS point clouds were processed using ArcMap software to produce a digital terrain model (DTM) for the 29 August TLS Survey and digital surface models (DSM) for the 25 April and 3 June TLS surveys. Scans were compiled into LAS Datasets by date, and re-projected into the NAD 1983 UTM Projected Coordinate System (EPSG:26913). Point classifications were performed in ArcMap: the snow surface was identified by a ground classification for the 25 April and 3 June Surveys, and vegetation and ground returns were identified for the 29 August survey. The ground arrivals classification in the LAS datasets for 25 April and 3 June surveys, and the first returns classification for 29 August survey were converted into raster format with 0.5 m resolution, producing DSMs. The ground return classification in the LAS datasets for 29 August survey was converted into raster format with 0.5 m resolution, producing a DTM. All rasters were aligned to the 29 August DTM for subsequent differencing. The 29 August DTM was differenced from the 25 April and 3 June DSMs, to produce spatially extensive snow depth maps for these dates. The 29 August DTM was differenced from the 29 August DSM to produce a vegetation height map.

3.8.2 Snow Depth-loss Distributed Maps

25 April and 3 June TLS scans were parsed out by time of acquisition and loaded into ArcMap. Following the methodology outlined in Section 3.8.1, the Meadow region was subsetted and reprojected into NAD 1983 Projected Coordinate System. A ground classification was run to identify the snow surface on all scans and converted into rasters with 0.5 m resolution. Rasterized scans acquired from 10:00-11:00 MDT were differenced from rasterized

scans acquired from 14:00-15:00 MDT. The TLS shifted to some degree throughout the scans. This was mostly corrected for during scan alignments, but some unrealistic depth loss values were still present. These were eliminated from the analysis, and the mean depth loss calculated to adjust snow depths acquired via depth probe.

3.9 Calculating Liquid Water Content

3.9.1 Probed Snow Depth Adjustments

For the 5 April survey, a dry-snow survey, radar-derived depths (using a velocity derived from the snowpit density and Equation 2.2) were compared with probe-derived depths. In nearly all cases, probe-measured depths were greater than GPR-derived depths (Figure 3.3a). There are several possible factors contributing to the observed disagreement: (1) the probe measured higher depths than the GPR due to over-probing, (2) the true snow density was less than the observed snowpit density, or (3) void spaces existed around vegetation near the snow-ground interface. The mean Probe – GPR disagreement was calculated as 14 ± 2 cm at the 95% confidence interval established using the t-distribution (Figure 3.3b). The uncertainty of snow depth probes is ± 5 cm (Sturm and Holmgren, 2018), with a higher likelihood of over-probing in the observed thawed and saturated soil conditions.

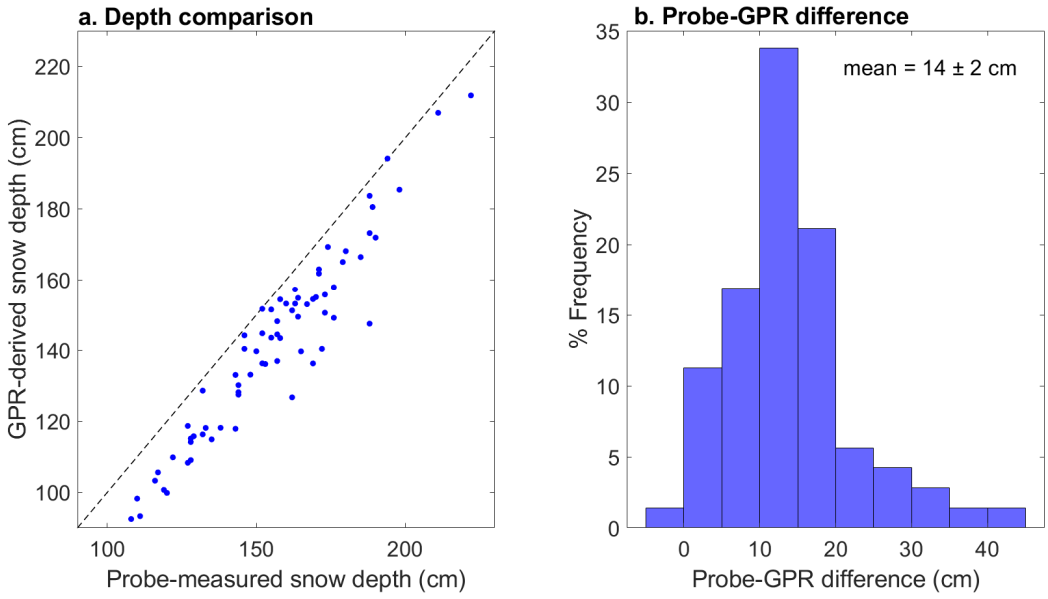

Figure 3.3: (a.) Probe-measured snow depth compared to GPR-derived snow depths. GPR-derived snow depths were calculated using bulk snow density measured in the snowpit and Equation 3.6. (b.) Histogram for the difference between probe-derived snow depths and GPR-derived snow depths. Confidence interval calculated using the t-distribution.

The probe-derived velocity for 5 April is 0.254 m ns^{-1}, which contrasts with the density-derived velocity of 0.229 m ns^{-1}. To further investigate the source of the probe – GPR disagreement, the velocity space for Equations 2.8 and 3.6 was plotted against decreases in density from the observed 360 kg m^{-3} and decreases in probed-depth (Figure 3.4). Where velocity difference is 0 m ns^{-1}, the equations agree perfectly. If the probed depth error is 0 cm, then the density error must be −150 kg m^{-3} for perfect agreement between the velocity equations. If the density error is assumed to be 0 kg m^{-3}, then the probe error must be −14 cm for perfect velocity agreement. Given the relatively low uncertainty (1-6%) for density measurements using wedge cutters (Proksch et al., 2016; Lopez-Moreno et al., 2020), it is easier to explain the velocity differences by assuming the probe as the sole source of error and then adjust the probed-snow depths accordingly.

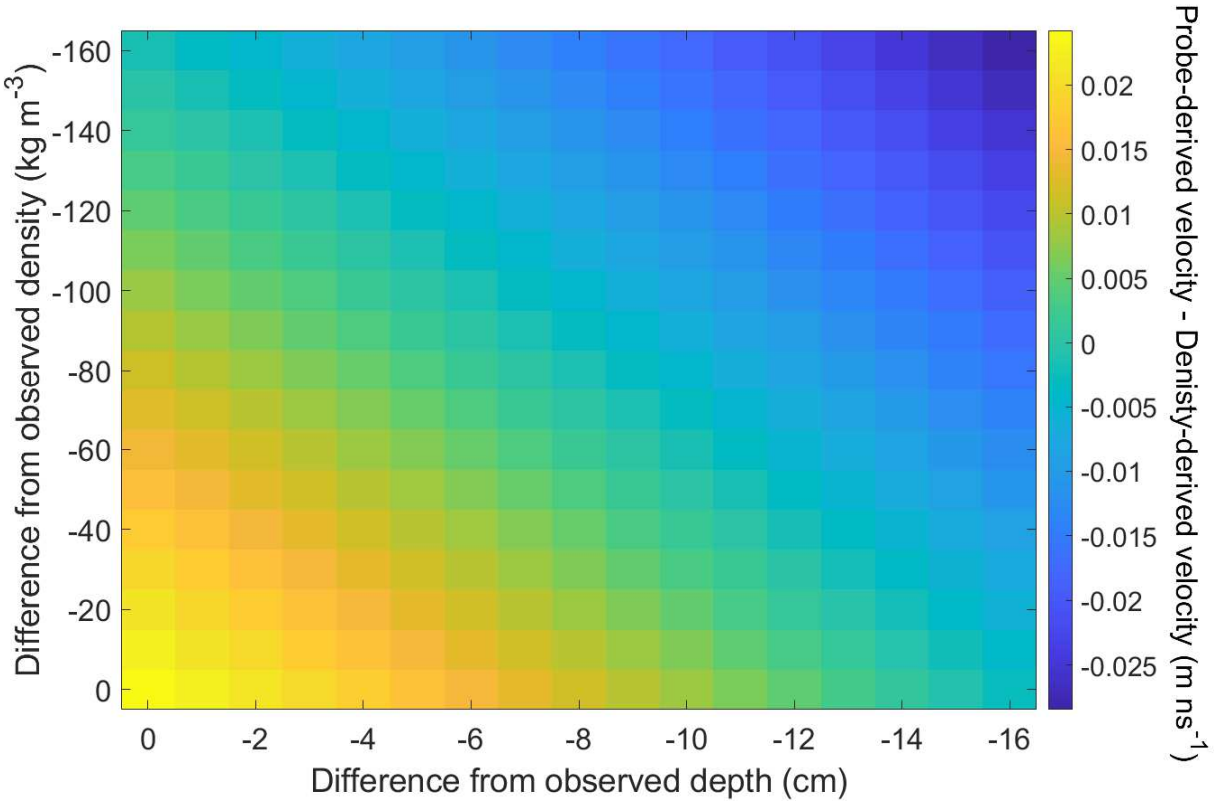

Figure 3.4: Plot of density-derived velocity (Equation 3.6) subtracted from probe-derived velocity (Equation 2.8). Where velocity difference is 0 m ns^{-1}, the equations are in perfect agreement. Probe-derived velocity is displayed as the function of the 5 April mean probed snow depth minus increments of depth. Density-derived velocity is displayed as a function of the 5 April bulk snow density minus increments of density.

The suggested −14 cm probe-error is nearly three times larger than the probe uncertainty. Over-probing into unfrozen soil is possible, but a consistent 14 cm of over-probing is unlikely. LiDAR-derived vegetation heights from the 29 August LiDAR survey were plotted as a histogram for the Meadow and South Transects (Figure 3.5). The mean vegetation heights for the Meadow and South Transects are 24.4 cm and 21.0 cm, respectively. The development of void spaces around vegetation is possible but would result in substantial density anomalies, and given the analysis presented in Figure 3.4 and the wedge cutter uncertainty, this is unlikely. Thus, it is suggested that the thick vegetation observed at Cameron Pass is compressed by the overlying

mass of the snowpack (e.g., Pomeroy et al., 2006) and comprises a mat at the base of the snow that is penetrated by the depth probe.

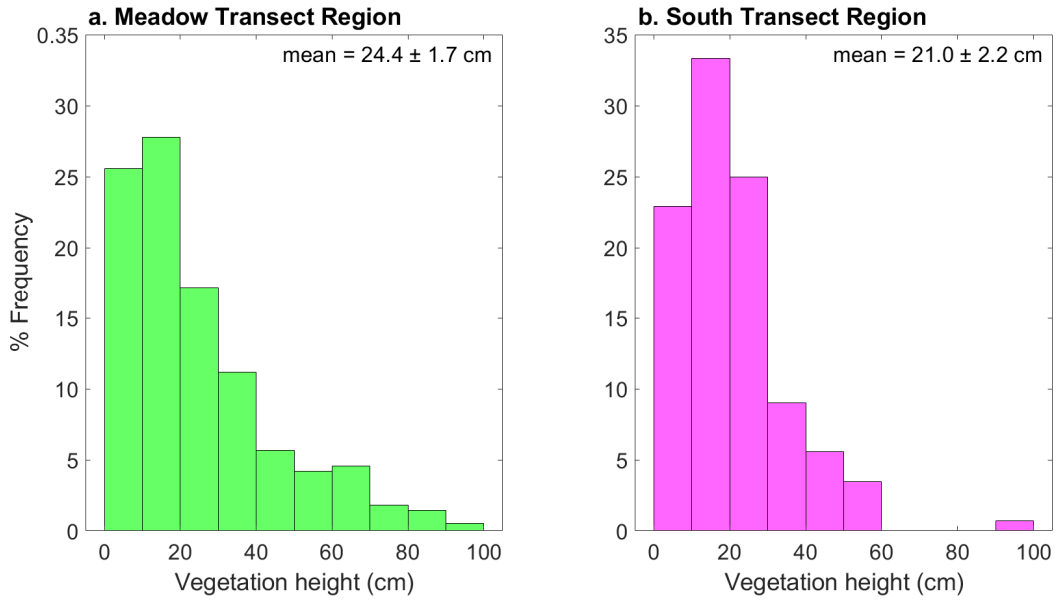

Figure 3.5: LiDAR derived vegetation heights from 29 August TLS survey for (a.) Meadow Transect and (b.) South Transect. Confidence interval calculated from t-distribution.

3.9.2 Snow Depth-loss Calculations

Transects were surveyed for snow depth during the morning survey, but snow ablation was observed in the snowpits for several survey dates and snow depth likely decreased throughout the day on those survey dates. Thus, in order to accurately calculate LWC, snow depths need to be adjusted for each GPR survey. Using the Joe Wright SNOTEL station, hourly snow depths, which have a precision of 2.54 cm (Ryan et al., 2008), were regressed to test a statistically significant depth-loss slope (Figure 3.6). The 10 June regression has an $R^2 = 0.441$ and a slope estimate = -0.59 cm hr^{-1}. The 19 June regression has an $R^2 = 0.563$ and a slope estimate of -0.60 cm hr^{-1}. Regressions for other survey dates did not show a strong statistical relation for depth-loss and were not used.

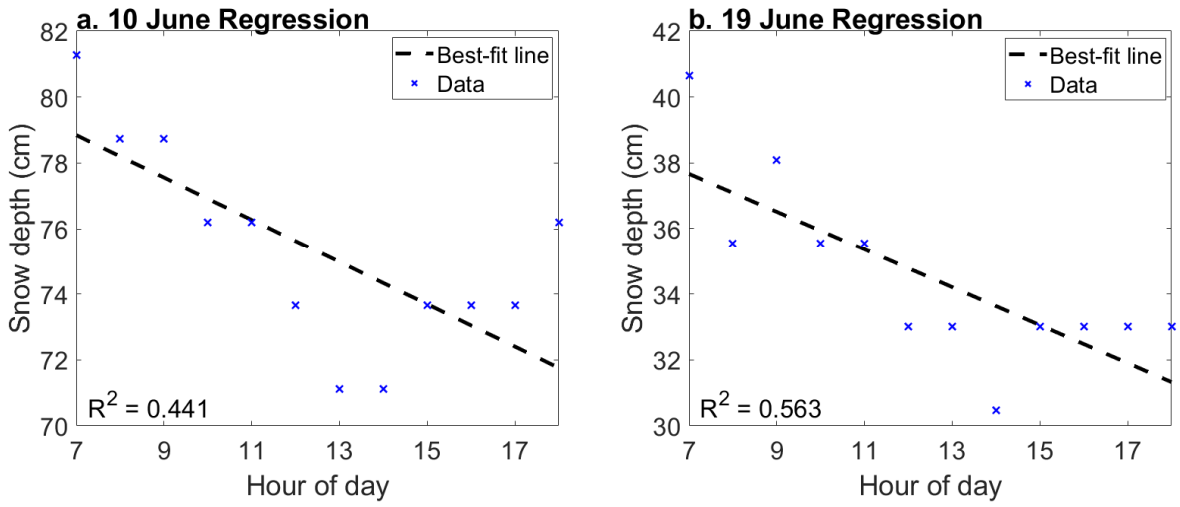

Figure 3.6: Regression analysis for snow depth-loss on 10 June (a.) and 19 June (b.) at Joe Wright SNOTEL station. Regression performed on hourly snow depth data between 08:00 and 18:00 MDT.

On 25 April and 3 June, the Meadow Transect region was captured by TLS between 10:00-11:00 MDT and again between14:00-15:00 MDT. Rasters for these scans were differenced, providing distributed maps for snow depth-loss on those dates. The mean depth-loss for 25 April (−2.57 cm) and for 3 June (−2.48 cm) were subtracted from the Meadow and South Transect probed depths for the afternoon and evening surveys (Figure 3.7). Depth was altered for the North Transect; the North Transect is similar in terms of LAI and NI to the Joe Wright SNOTEL station, which saw negligible depth loss on those dates.

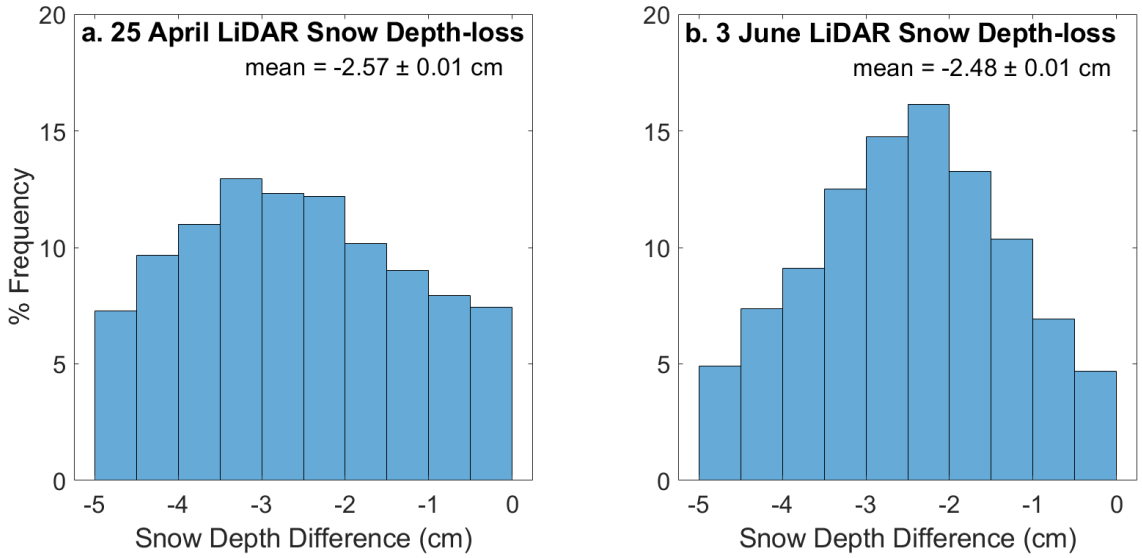

Figure 3.7: Histograms for the snow surface height difference between morning (10:00-11:00 MDT) and midday (14:00-15:00 MDT) TLS surveys. (a.) Snow depth-loss for 25 April TLS survey. (b.) Snow depth-loss for 25 April TLS survey. Confidence interval calculated using t-distribution.

3.9.3 Constraining Radar Velocity to Calculate LWC

To calculate LWC from probe-derived snow depths, depth measurements were corrected by subtracting the mean depth disagreement (14 cm). Then, a starting point was identified for each transect. Depth measurements and *twt*, beginning with the probed depth closest to the starting point, were averaged over 9 m intervals. The mean LiDAR-derived snow depth loss was applied to 25 April and 3 June midday and evening surveys for the depths acquired along the Meadow and South Transects. Regressed snow depth-losses were applied to 10 June and 19 June depth measurements for the midday and evening surveys. Radar velocity was calculated (Equation 2.8) along each transect using depth and *twt* calculated along 9 m intervals. Permittivity was calculated from the radar velocity (Equation 2.1). Finally, LWC was calculated from transect-specific snowpit density and depth-derived permittivity (Equation 3.7). The only exceptions for the use of transect-specific density included the 5 April survey, where the

Meadow Transect density was used for all transects, and the 25 April survey, where the Meadow Transect used the average of the North and South Transect densities.

To calculate LWC from LiDAR derived snow depth, the 29 August DTM was differenced from the 25 April and 3 June DSMs to produce distributed snow depth maps for 25 April and 3 June. For these dates, GPR was pulled along spirals in the Meadow and South Transect regions during the morning and midday survey, coinciding with the TLS scanned regions. In ArcMap, *twt* was converted to raster-format at 0.5 m resolution and aligned to the 29 August DTM. Radar velocity was calculated for the overlapping *twt* and depth pixels (Equation 2.8). Permittivity was then calculated from the radar velocity (Equation 2.1) and LWC was calculated from snowpit density and depth-derived permittivity Equation 3.7) to generate 0.5 m gridded LWC for morning and evening surveys.

3.9.4 Statistical Analyses

LAI and NI were binned for the 9 m LWC intervals. Single-variable linear regressions were applied to individual survey dates to relate % vol. LWC to LAI and NI. Positive degree days (PDD; Wake and Marshall, 2015; Equation 3.8), a proxy for available melt energy, were calculated using Joe Wright SNOTEL station hourly temperature data. PDD is the scaled cumulative sum of positive hourly temperatures, where t is the time in hours after 00:00 MDT and T is a positive temperature (°C) at time t. LWC measured along the North, Meadow, and

$$PDD = \frac{1}{24}\sum_{t=0}^{t} T_t \, , where \; T_t > 0 \; ℃ \qquad \text{(Equation 3.9)}$$

South Transects and PDD at the time of the survey were differenced – midday minus morning and evening minus midday – to find the change in LWC (ΔLWC) and change in PDD (ΔPDD). These datasets were grouped by survey date and into a ΔLWC time-series dataset. Finally, a

multi-variable linear regression analysis was run for each survey date and the time-series dataset to compare ΔLWC with LAI, NI, ΔPDD, the product of LAI and NI (LAI x NI), the product of LAI and ΔPDD (LAI x ΔPDD), and the product of NI and ΔPDD (NI x ΔPDD).

3.10 Radar SWE-retrieval Methodology

Reductions in radar velocity, caused by LWC, are a primary source of uncertainty for L-band radar SWE-retrievals during the melt season. In the western U.S., SNOTEL stations provide real-time density observations that can be leveraged to improve dry-snow radar SWE-retrievals. Currently, SNOTEL stations are unequipped to provide direct measurements of LWC; density measurements without an LWC measurement underestimate permittivity, thereby overestimating SWE (Figure 2.1c). To assess this uncertainty, a baseline for true SWE was established using probed snow depths and snowpit-measured densities (Equation 2.4). Then, snow depths were calculated with the assumption of dry-snow densities (Equation 2.2) and *twt* (Equation 2.3). The dry-snow density assumption neglects the velocity attenuation effects of LWC. Snowpit-measured densities and Joe Wright SNOTEL densities were used to calculate separate snow depth profiles for the same *twt* profile. Radar SWE-retrievals were calculated from the radar-derived depths (Equation 2.4). The mean SWE was calculated for both the radar SWE-retrievals that used snowpit-measured densities and the radar SWE-retrievals that used Joe Wright SNOTEL densities and compared with the mean probe-derived SWE.

4. Results

4.1 Overview of the Study Period

The observation period began on 5 April 2019 and ended on 19 June 2019. In the snowpit for the 5 April survey, the mean snow temperature (taken at 10 cm intervals) was −0.9°C and ice lenses were absent, but a ~3 cm melt-freeze crust was present at the surface. LWC measurements taken at 10 cm intervals with the SLF Snow Sensor were consistently 0 vol. %. Thus, the 5 April survey is considered a dry-snow survey. Melt water was observed on all subsequent surveys.

Peak SWE, observed by the Joe Wright SNOTEL station, occurred on 18 April, SWE remained within 20% of peak SWE until 7 June, and full melt-out was observed on 30 June (Figure 4.1a). The melt season (Equation 3.3) lasted 73 days for the 2019 season, which is significantly longer than the 1978-2018 average of 46 days. The longer 2019 melt season can be attributed to lower average daily temperatures and six late-season storm events which are identifiable in Figure 4.1a and each increased snow surface albedo by adding >10 mm of SWE (Table 4.1). April-June temperatures were consistently lower than the 2009-2018 average temperatures (Figure 4.1a), with the April-June 2019 median air temperature being 1°C cooler than the April-June 2009-2018 median air temperature.

Table 4.1: Significant late-season storm events recorded at the Joe Wright SNOTEL Station for the 2019 season.

	30-Apr	**18-May**	**21-May**	**29-May**	**20-Jun**	**22-Jun**
Precipitation (mm)	23	15	13	15	20	13
SWE (mm)	25.4	10.2	20.3	12.7	0.0	20.3

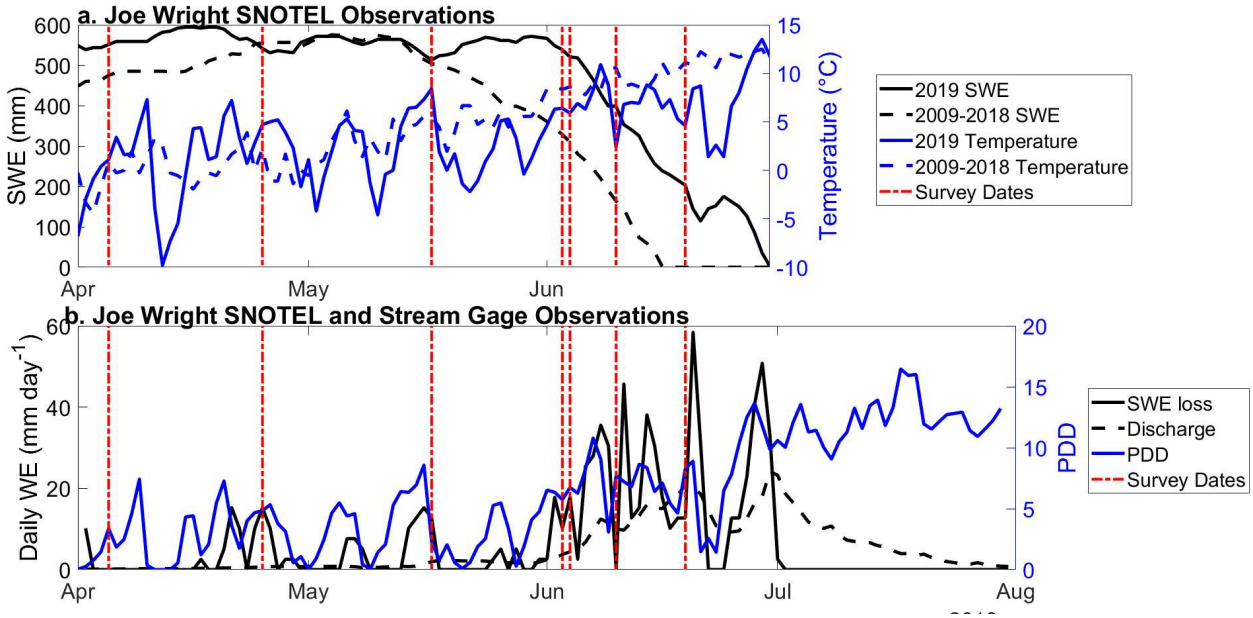

Figure 4.1: (a.) Joe Wright SNOTEL station 2019 daily observations of SWE and average air temperature, compared with 2009-2018 daily averages. (b.) Joe Wright SNOTEL station 2019 hourly observations of air temperature, converted to PDD, compared with SWE loss from Joe Wright SNOTEL station and stream discharge from Joe Wright Creek stream gage, converted to water equivalent (WE). Michigan Ditch stream gage data was subtracted from Joe Wright stream gage to remove regulated inflow.

Between 18 April and 31 May, there was negligible SWE loss and associated discharge (Figure 4.1b). Discharge and SWE loss are positively correlated with PDD (Figure 4.2). Night-time temperatures were not consistently warmer than 0°C until June, at which time PDDs increased substantially, marking the beginning of significant SWE loss and stream discharge. Stream discharge and SWE loss are positively correlated (Figure 4.2c), with discharge exhibiting a smoother curve than SWE loss (Figure 4.1b).

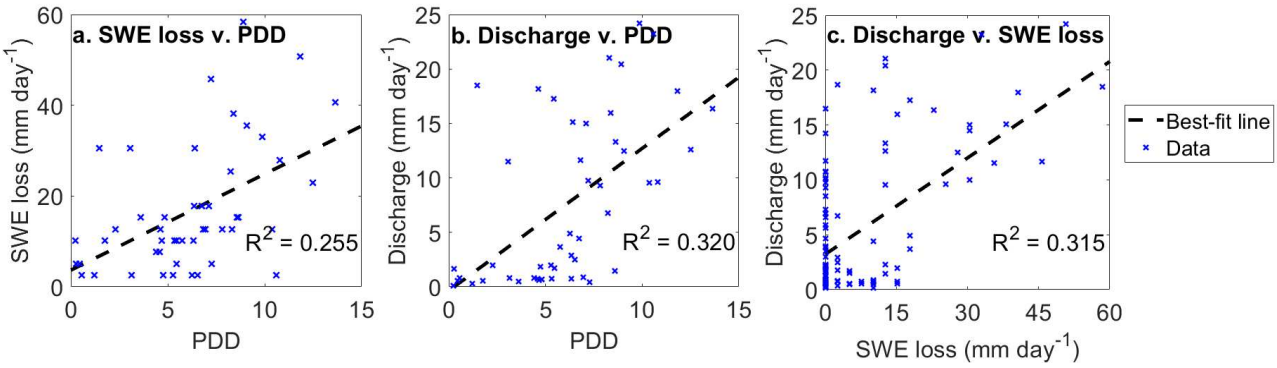

Figure 4.2: (a.) Correlation between SWE loss and PDD. (b.) Correlation between discharge and PDD. (c.) Correlation between discharge and SWE loss. Discharge data normalized using basin area from Joe Wright Stream gage. SWE loss and PDD calculated from Joe Wright SNOTEL station.

4.2 In-Situ Observations

For each survey date, manual snow depth measurements were acquired at 3 m intervals using a probe at the start of the day (Figure 4.3). Due to time constraints, depth transects for three dates covered a limited portion of the full transect (Table 3.1). Snow depths decreased from one survey date to the next and the highest median snow depths were observed on the North Transect (Figure 4.4a). Median North Transect snow depth values decreased for all survey dates from 5 April to 19 June. Depth distributions on the Meadow (Figure 4.3b) and South (Figure 4.3c) Transects displayed similar ranges and medians. Median snow depth values on the Meadow Transect decreased for all survey dates from 5 April to 10 June (Figure 4.4b). Median South Transect snow depth values decreased for survey dates from 5 April to 3 June, after which the median snow depth increased by 1.5 cm from 3 June to 4 June, even though precipitation was not observed at the SNOTEL station. Higher snow depths were observed on the first 25 m of the north ends of the Meadow and South Transects, possibly as a result of snowplow operations on CO-14 and snow blowing off the edges of the road.

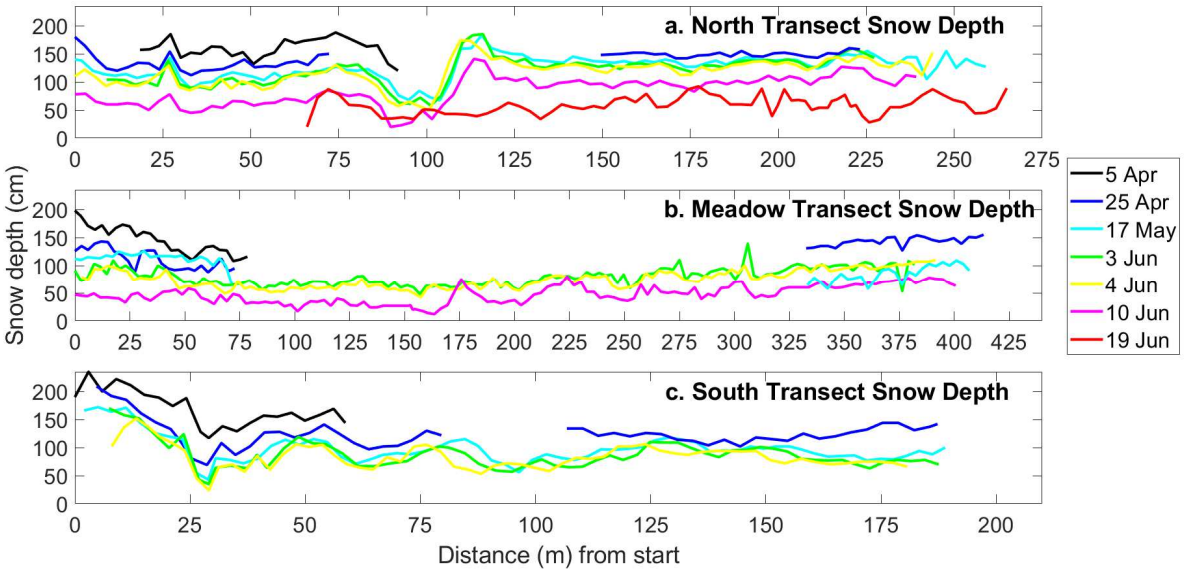

Figure 4.3: Snow depth measurements on the (a.) North Transect, (b.) Meadow Transect, and (c.) South Transect. Snow depths on 5 April (a., b., & c.), 25 April (a., b., & c.), and 17 May (b.) surveys were acquired on a subset of the transect. Transects varied slightly in length throughout the survey period.

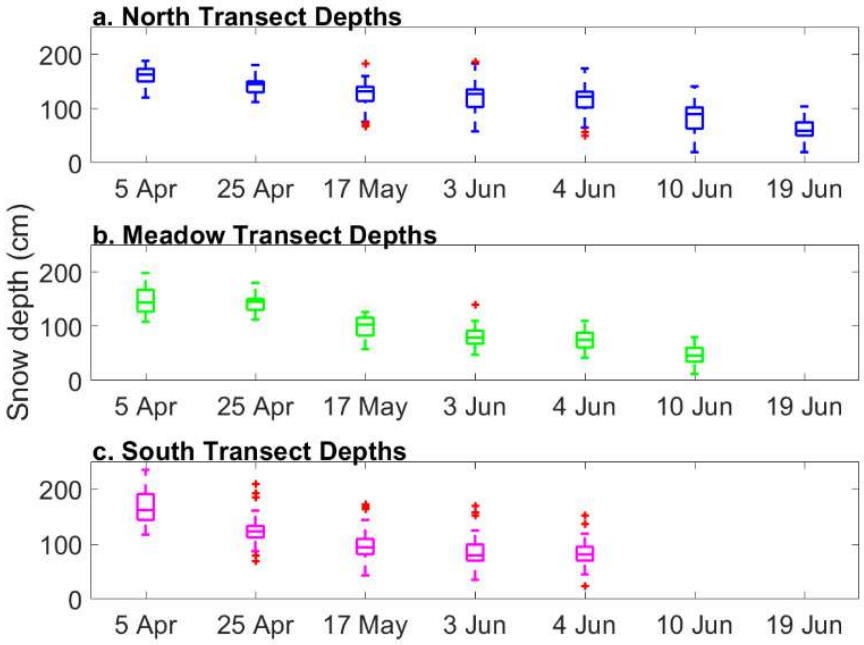

Figure 4.4: Boxplots displaying snow depth variability for the (a.) North, (b.) Meadow, and (c.) South Transects. The boxes extend to the upper and lower quartiles, while the whiskers extend to extreme values not considered outliers. Red crosses denote outliers.

Density and LWC were measured (Figure 4.5) in snowpits dug at the northern end of the North Transect in an area with higher canopy cover (Figure 3.1a). Bulk density measurements

generally increased from 25 April to 19 June and followed the Joe Wright SNOTEL density observations closely (mean difference = 5.7%). There is one significant discrepancy in the density measurements: the density measured on 4 June is 35.6 kg m^{-3} greater than the density measured on 3 June (7.7% difference). The Joe Wright SNOTEL station observed a density increase of 5 kg m^{-3} between 3 June and 4 June, but this does not fully explain the discrepancy. There were two important differences between the two snowits. The 3 June snowpit was dug ~20 m to the south of the 4 June snowpit, in a more open canopy environment. Additionally, three ice lenses of thicknesses up to 5 cm were observed in the 4 June snowpit, whereas the 3 June snowpit lacked ice lenses (Figure 4.6). It is notoriously difficult to measure the density of a layer with one or more ice lenses with a wedge cutter; the hardness of the ice contrasts strongly with the surrounding snow and density is usually misrepresented, so it is possible that the 4 June density measurement is an outlier. SLF LWC measurements increased from the morning survey to the evening survey on 25 April and 10 June, but decreased from morning to evening on 3 June, 4 June, and 19 June (Figure 4.5b). LWC peaked on the midday surveys of 4 June and 19 June. The highest SLF measured LWC (8.5%) occurred on the 19 June midday survey, when standing water was observed at ~5 cm height at the base of the snowpit.

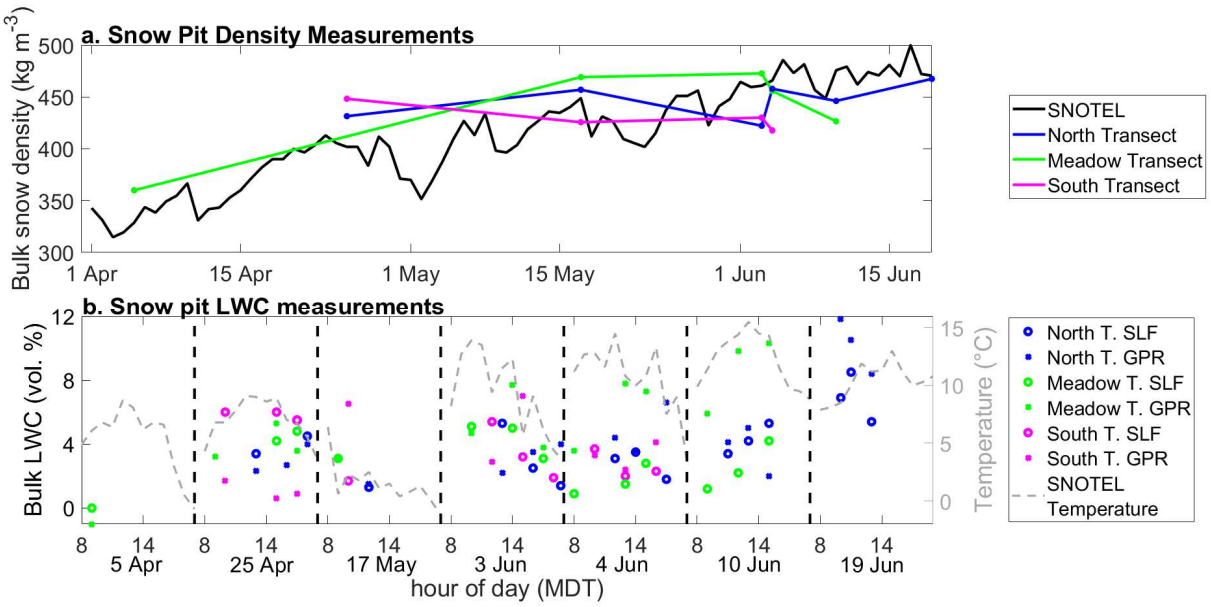

Figure 4.5: (a.) Snowpit density measurements compared with Joe Wright SNOTEL station density observations. (b.) LWC observations categorized by time-of-day obtained in snowpits by the capacitive SLF Snow Sensor and GPR. GPR LWC calculated ~1 m from SLF measurements. The Meadow Transect snowpit was the only snowpit dug for 5 April.

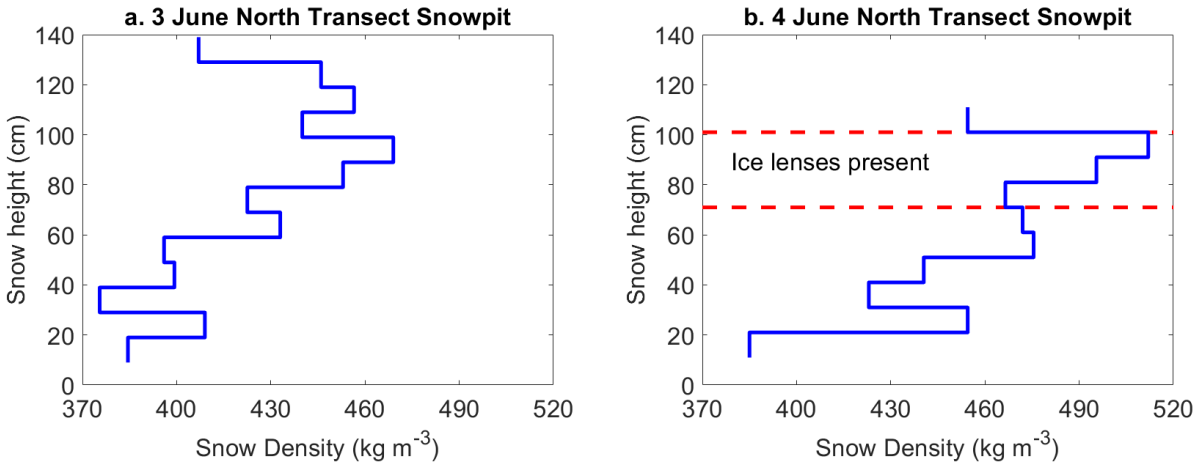

Figure 4.6: Snow density observed along 10 cm intervals in snowpits on the North Transect on (a.) 3 June and (b.) 4 June.

For the Meadow Transect, density measured on 25 April was 546 kg m^{-3}, which was anomalously high and likely erroneous. Thus, it was not used, and it was replaced with the average of the 25 April densities measured on the North and South Transects. The 5 April density was the lowest measured (360 kg m^{-3}), which is indicative of dry-snow prior to melt-

driven densification. Meadow density peaked on 3 June and decreased with each subsequent survey. The 3 June and 4 June surveys differ by 16.9 kg m^{-3} (3.7% difference). Meadow Transect densities follow Joe Wright SNOTEL station observed density closely (mean difference = 5.5%), with the strongest disagreement occurring late in the melt season (11.1% difference for 10 June). The highest LWC was observed on 3 June (5.1%). LWC increased from morning to evening on 4 June and 10 June. LWC never peaked on the midday surveys. Lower LWC was observed on the 10 June morning survey – on this date, the upper 23 cm of the Meadow Transect snowpack had frozen solid due to sub-freezing overnight temperatures (minimum air temperature = −5.1°C).

The highest density observed on the South Transect was recorded on 25 April at 448 kg m^{-3}, and density generally declined for the remaining surveys. 3 June and 4 June density measurements agree within a 2.9% difference. South Transect densities show different trends and values than the Joe Wright SNOTEL station observations (mean difference = 8.5%). Snowpit LWC decreased from morning to evening for 25 April, 3 June, and 4 June surveys.

4.3 Uncertainties for In-Situ Observations

The in-situ snow observation methods employed in this study have known uncertainties associated with their measurements. The uncertainty for probed snow depths is ±0.05 m (Sturm and Holmgren, 2018), with a higher likelihood of over-probing in unfrozen ground conditions. Additionally, the location of probed depths has two primary sources of uncertainty: ±0.25 m from the geolocation process and ±0.5 m from the accuracy of the PPK solution. The wedge cutter, used to measure snow density, can underestimate snow density by 1-6% in dense snow due to incomplete sampling (Proksch et al., 2016). For nearly all snowpits, significant vegetation protruded in the lower 20 cm which prevented the acquisition of density samples, potentially

biasing the bulk density calculations. Snowpit LWC measurements were acquired with a SLF Snow Sensor, which estimates LWC from the permittivity of the snow. This instrument has yet to be tested outside of the WSL Institute for Snow and Avalanche Research in Davos, Switzerland, and its uncertainty has not been formally quantified. Any attempt at replicating a measurement resulted in a lower subsequent LWC estimate. Since the capacitive plate is placed on the surface of the snowpit face, perhaps the plate removes water from the snow face, reducing subsequent measurements. Measurements taken along the same layer often resulted in LWC measurements that differed by up to 7 vol. %. Thus, SLF Snow Sensor measurements are used cautiously for comparison with LWC trends identified by GPR measurements.

4.4 GPR Measurements of LWC using Depth Probes

Following the methods outlined in Section 3.7.3, LWC was calculated for the three transects and explainable outliers were removed from the analysis. LWC calculated along the North Transect (Figure 4.7a) was 0 vol. % on 5 April and progressively increased throughout the observation period. Median values for morning surveys (Table 4.2) increased from 5 April to 3 June, decreased from 3 June to 10 June, and increased for 19 June. The median ΔLWC (Figure 4.7b) from morning to midday was positive on 25 April (+0.2 vol. %) and 10 June (+1.1 vol. %), negative on 4 June (−0.8 vol. %), and 19 June (−0.2 vol. %), and negligible on 3 June (0 vol. %). The median ΔLWC from midday to evening was negative on all dates. The range in ΔLWC increased after 25 April. LWC magnitude exhibited spatial consistently, with regions of higher LWC early in the observation period continuing to show higher LWC later in the observation period, and vice versa. The highest LWC values were observed on 19 June (12 vol. %).

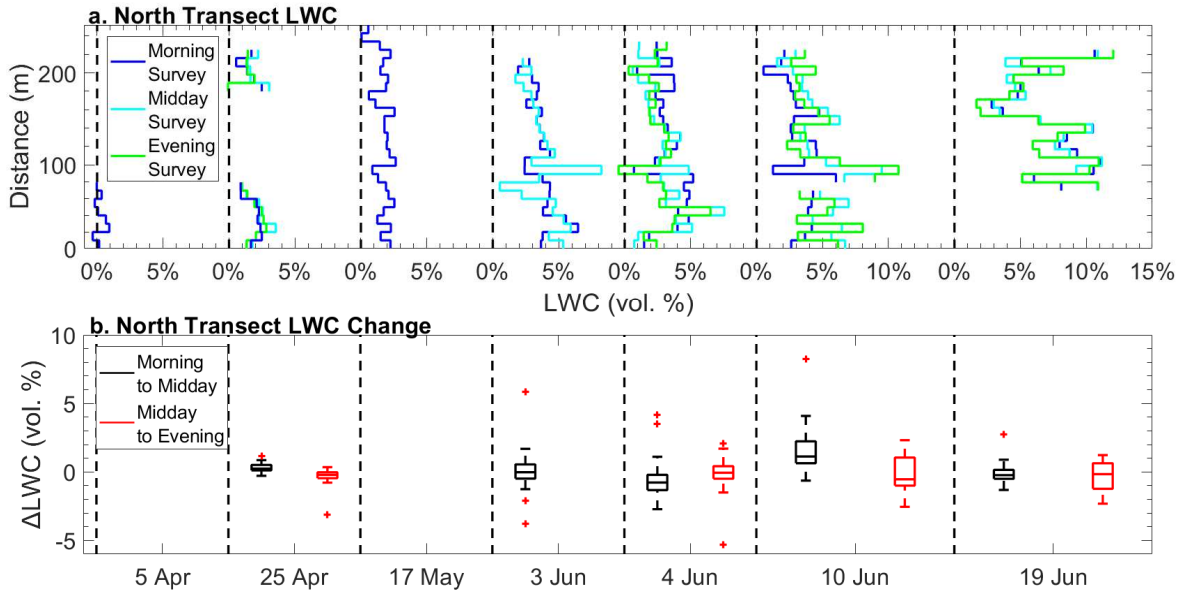

Figure 4.7: (a.) North Transect LWC averaged along 9 m intervals for morning, midday, and evening surveys, compared to distance along transect. Explainable outliers were removed and are represented as breaks in the line. (b.) Boxplots for ΔLWC along the North Transect from morning to midday and from midday to evening, where positive values represent an increase in LWC and negative values represent a decrease in LWC. Only one survey was performed on 5 April and 17 May. The 3 June evening survey GPR track did not have a base station file for which to apply PPK, causing it to exhibit exceptionally poor GPS quality, and was not included in the analysis.

LWC calculated along the Meadow Transect (Figure 4.8a) was 0 vol. % on 5 April and progressively increased throughout the observation period. Median values for morning surveys (Table 4.2) increased from 5 April to 17 May, decreased from 17 May to 3 June, and increased from 3 June to 10 June. The median ΔLWC (Figure 4.8b) from morning to midday was positive on 25 April (+0.8 vol. %), 3 Jun (+1.6 vol. %), and 10 June (+1.2 vol. %), and negligible on 4 June (~0 vol. %). The median ΔLWC from midday to evening was negative on all dates. The range in ΔLWC increased significantly on the 10 June surveys. LWC is consistently higher in the northern and southern ends of the transect but can be high or low in the middle region, where the transect crosses the Michigan River twice. The highest LWC values were observed on 10 June (maximum = 19.7 vol. %), near the Michigan River.

Table 4.2: Median vol. % LWC for the North, Meadow, and South Transects for morning surveys.

	North Transect	Meadow Transect	South Transect
5-Apr	0.1 vol. %	-0.1 vol. %	0 vol. %
25-Apr	2.0 vol. %	1.7 vol. %	1.6 vol. %
17-May	1.8 vol. %	2.9 vol. %	2.8 vol. %
3-Jun	3.7 vol. %	2.7 vol. %	3.8 vol. %
4-Jun	3.3 vol. %	3.4 vol. %	4 vol. %
10-Jun	3.0 vol. %	6.9 vol. %	Melt-out
19-Jun	6.5 vol. %	Melt-out	Melt-out

LWC calculated along the South Transect (Figure 4.9) was 0 vol. % on 5 April and progressively increased throughout the observation period. Median values for morning surveys (Table 4.2) increased with each subsequent survey. The median ΔLWC (Figure 4.9b) from morning to midday was positive on 25 April and negative on 3 June, and 4 June. The median ΔLWC from midday to evening was negative on all dates. The highest LWC values were observed on 3 June (maximum = 10.8 vol. %), on a forested, south-facing slope at ~60 m distance from the western terminus of the transect. Higher LWC values were consistently observed in this region, which is an area where surface slopes are lower and the transect breaks from the forest and moves into the meadow

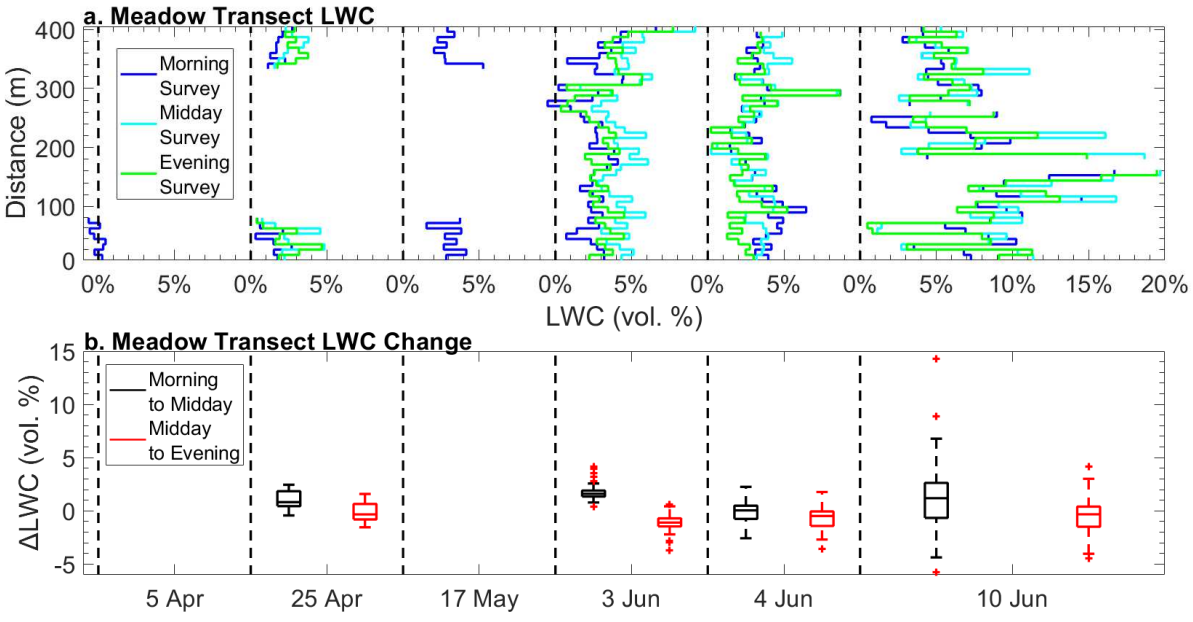

Figure 4.8: (a.) Meadow Transect LWC averaged along 9 m intervals for morning, midday, and evening surveys, compared to distance along transect. Explainable outliers were removed and are represented as breaks in the line. (b.) Box plots for ΔLWC along the Meadow Transect from morning to midday and from midday to evening, where positive values represent an increase in LWC and negative values represent a decrease in LWC. Only one survey was performed on 5 April and 17 May.

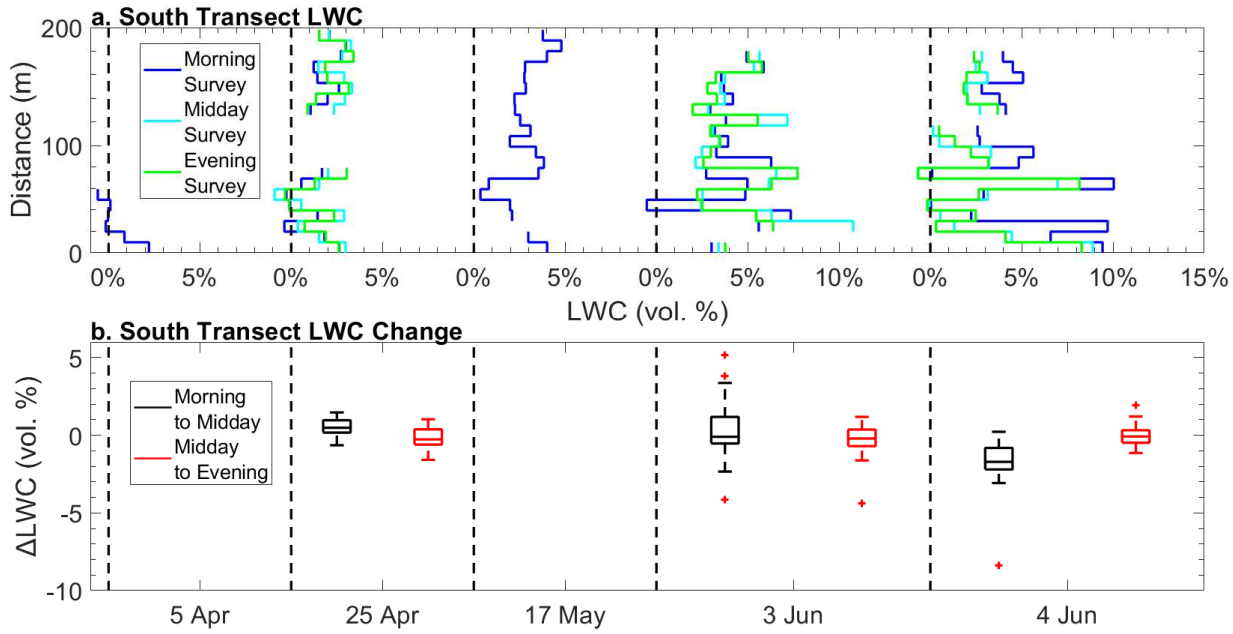

Figure 4.9: (a.) South Transect LWC averaged along 9 m intervals for morning, midday, and evening surveys, compared to distance along transect. Explainable outliers were removed and are represented as breaks in the line. (b.) Box plots for ΔLWC along the South Transect from morning to midday and from midday to evening, where positive values represent an increase in LWC and negative values represent a decrease in LWC. Only one survey was performed on 5 April and 17 May.

4.5 Uncertainties in GPR Measurements of LWC using Depth Probes

Sources of uncertainty for GPR-derived LWC include probe uncertainty, sled compression, and a persistent, albeit compressed, vegetation layer at the base of the snowpack. Sled compression resulted in a maximum snow depth reduction 0.00-0.05 m (prior to melt-driven densification, low-density snow at the surface can result in higher sled compression), and slight modification of the density. Sled compression of 0.05 m can lead to a 5.3% increase in density for a 1 m snowpack with 400 kg m^{-3} initial density. Sled compression is not expected to be a significant source of uncertainty, given the analysis presented in Figure 3.4. As calculated in Section 3.9.1, the persistent compressed vegetation layer, combined with the probe uncertainty

and sled compression is estimated to reduce measured snow depth by an average of 0.14 ±0.02 m at the 95% confidence interval, using a t-distribution. The confidence interval results in an uncertainty for LWC measurements of ±1.5 vol. %.

4.6 Statistical Analysis Results

LAI was calculated for the 9 m probe intervals and compared with LWC using single-variable linear regressions (Figure 4.10). The Meadow Transect and any LWC values with LAI < 0.4 were removed from this analysis. The 5 April survey contains the fewest points, as only a section of the transects were probed. The South Transect melted out before 10 June, so 10 June and 19 June surveys contain data from the North Transect only. LWC is negatively correlated with LAI on all surveys except 3 June morning (Figure 4.10d), midday (Figure 4.10i), and evening (Figure 4.10n) surveys, and 4 June evening (Figure 4.10o) survey. The magnitude of best-fit line slopes varied by date but were mostly consistent within the surveys performed on that survey date. The most negative slopes occur on 25 April and 19 June. The spread in data is tightest on 5 April, 25 April, and 10 June.

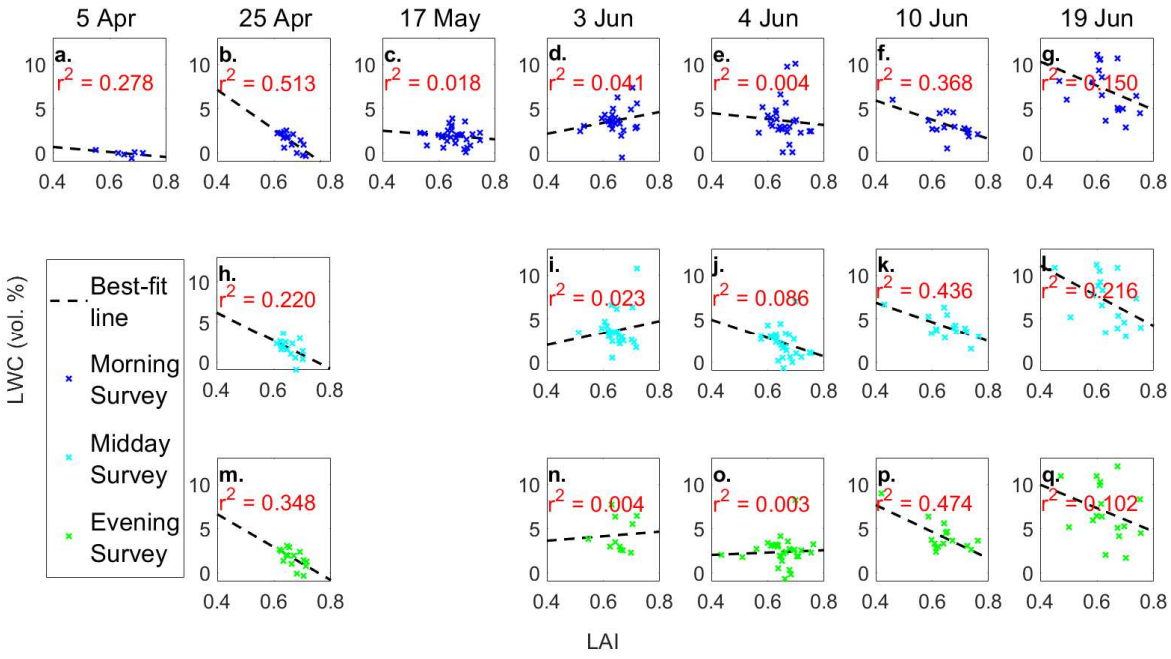

Figure 4.10: LWC compared to LAI. The Meadow Transect and all LAI values < 0.4 were removed for this analysis. 5 April scatter plot contains fewer data points because of the limited probing region. 10 June and 19 June scatter plots contain fewer data because the South Transect melted out before 10 June.

NI was calculated for the 9 m probe intervals and compared with LWC (Figure 4.11). All transects were used in the analysis. 5 April contains fewer data points due to the lower number of available probed points. There are two distinct groups on the scatterplots for 5 April through 4 June surveys; the negative NI group represents the South Transect and the near 0 NI group represents the North and Meadow Transects. Transect melt-out significantly reduced the number of 10 June scatter plot does not contain data points from the South Transect. 19 June scatter plot only contains data points from the North Transect. This dataset suggests a significantly lower degree of correlation between NI and LWC than LAI and LWC. In theory, the correlation should be negative, but most best-fit lines have a slope near 0 and r^2 values that are less than 0.100. Data spread is tighter for the datasets that contain both the South and North Transects, allowing for a more complete representation of possible NI values.

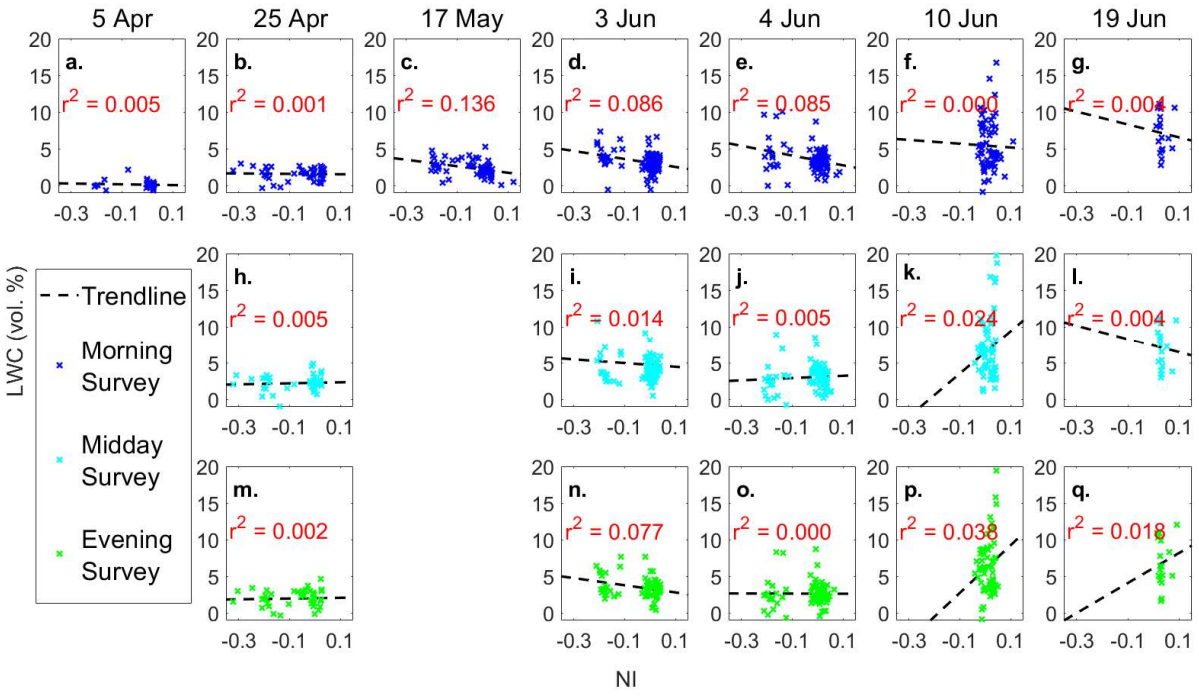

Figure 4.11: LWC compared to NI. All available transects are included in the analysis. 5 April scatter plot contains fewer data points because of the limited probing region. 10 June and 19 June scatter plots contain fewer data because the South Transect melted out before 10 June and the Meadow Transect melted out before 19 June.

LAI, NI, and ΔPDD were standardized using a normal distribution and multi-variable regression was performed on each individual survey date's GPR dataset and on the GPR dataset spanning the full study period (Figure 4.12). The overall goal of this analysis is to quantify whether the independent variables of LAI, NI, and PDD can be used to predict ΔLWC. For the full dataset, statistically significant variables (p-value < 0.10) include LAI, NI, ΔPDD, and NI x ΔPDD. As expected, there is significant scatter and the r^2 for this regression is 0.182. In this multi-variable analysis, the coefficient for LAI is positive, whereas in the single-variable analysis (Figure 4.10) LAI showed a negative correlation with LWC. However, the LAI x ΔPDD coefficient is negative, which should represent short-wave attenuation by canopy cover. Therefore, the positive coefficient for LAI may be representative of a long-wave contributor to the snowpack energy balance. NI is shown to have a strongly negative estimate, which is

expected, but differs from the inconclusive relations derived from the single-variable analysis (Figure 4.11). The ΔPDD coefficient is low but has a positive sign. The sign of the ΔPDD coefficient is expected, but the magnitude is low in comparison to NI, as PDD is a proxy for the available melt-energy and NI is expected to modulate the available melt-energy. The NI x ΔPDD coefficient has a strongly positive contribution to ΔLWC. The sign of the estimate for NI x ΔPDD was expected to be negative, such that more southerly slopes are prone to higher short-wave influx.

The relations derived through multi-variable regression on individual survey dates approximates the relations derived from the full dataset, with some variation. Note, the 10 June and 19 June surveys do not contain LWC measurements from all three transects due to transects melting out, thus these survey dates contain the smallest range in LAI and NI. The LAI coefficient is positive and low-magnitude for all dates except 4 June, for which the coefficient is low-magnitude but negative. The 19 June survey date exhibits the only statistically significant LAI coefficient. The NI coefficient is low-magnitude with a negative slope on 25 April, 3 June, and 19 June, but switches to a low-magnitude positive coefficient for 4 June and 10 June. Only the 4 June NI dataset exhibits a statistically significant NI coefficient. The ΔPDD coefficient is low-magnitude and positive on 25 April, 3 June, and 19 June, high-magnitude but still positive on 10 June, and low-magnitude and negative on 4 June. The 25 April and 3 June datasets exhibited statistically significant ΔPDD coefficients. The LAI x NI coefficient is low-magnitude and negative on 25 April, 3 June, and 10 June, and low-magnitude and positive on 4 June and 19 June, with the estimate for 19 June being statistically significant. The LAI x ΔPDD coefficient is low-magnitude and negative for 25 April, 4 June, and 19 June, low-magnitude and positive for 3 June, and high-magnitude and positive for 10 June. No coefficients for LAI x ΔPDD are

statistically significant. The NI x ΔPDD coefficient is low-magnitude and negative for 25 April, 3 June, and 19 June, and low-magnitude and positive slope for 4 June and 10 June. Coefficients for NI x ΔPDD on 4 June and 10 June are statistically significant.

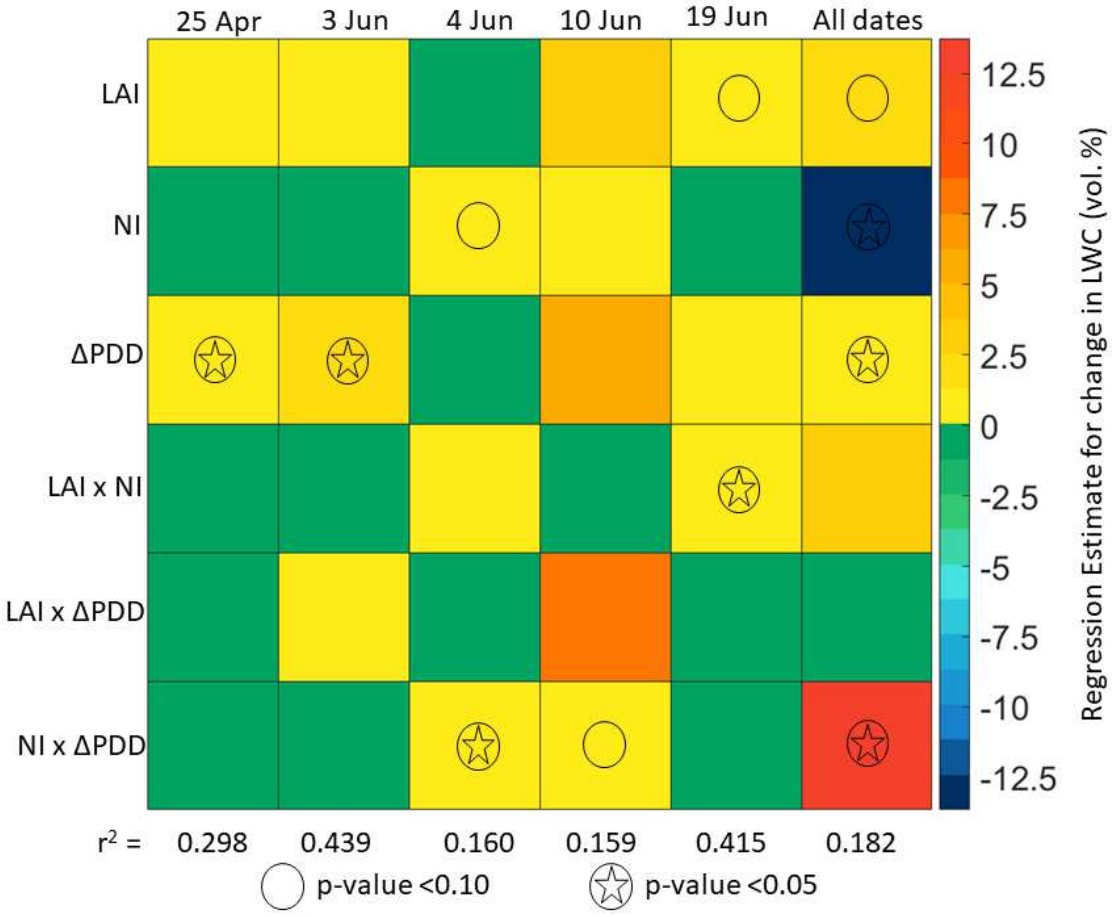

Figure 4.12: Multi-variable linear regression results for standardized LAI, NI, and ΔPDD. Columns represent datasets, with an r^2 listed at the base of each dataset, showing the fit of the regression estimates for that dataset. Rows represent individual variables. Estimates for variable slopes are shown by color. P-values calculated using the t-statistic for each variable.

4.7 Analyzing Radar SWE-retrievals

Radar SWE-retrievals were calculated using *twt* and either snowpit-measured densities or Joe Wright SNOTEL densities (Figure 4.13), which neglected the velocity attenuation effects of LWC. In all wet-snow scenarios (surveys conducted after 5 April), the dry-snow density model for permittivity overestimated SWE. The most egregious differences occurred late in the melt

season, when LWC was at its highest, resulting in a mean SWE overestimation by 40%. Joe Wright SNOTEL density observations were most similar to the North Transect. On 5 April, radar SWE-retrievals using snowpit-measured density compare well with the true SWE baseline (mean SWE-error = 1.3% and SWE-retrievals using Joe Wright SNOTEL density also compare favorably (mean SWE-error = −5.5%). The underestimation for the SWE-retrieval using SNOTEL density is attributed to the difference between SNOTEL density and snowpit density, of which the SNOTEL density is 32 kg m^{-3} less than the snowpit density. For other dates, the comparison between SWE-retrievals using snowpit density and SNOTEL density is more complex. In most cases, SWE-retrievals using SNOTEL densities are closer to the true SWE. This difference is caused by a difference between SNOTEL density and snowpit density. For most of the survey period, snowpit densities were less than SNOTEL densities. Thus, SNOTEL densities result in a higher permittivity value and a lower velocity, yielding mean SWE estimates that are closer to the true SWE baseline. In the cases where snowpit densities are higher than SNOTEL densities, SWE-retrievals suing snowpit densities are closer to the true SWE baseline.

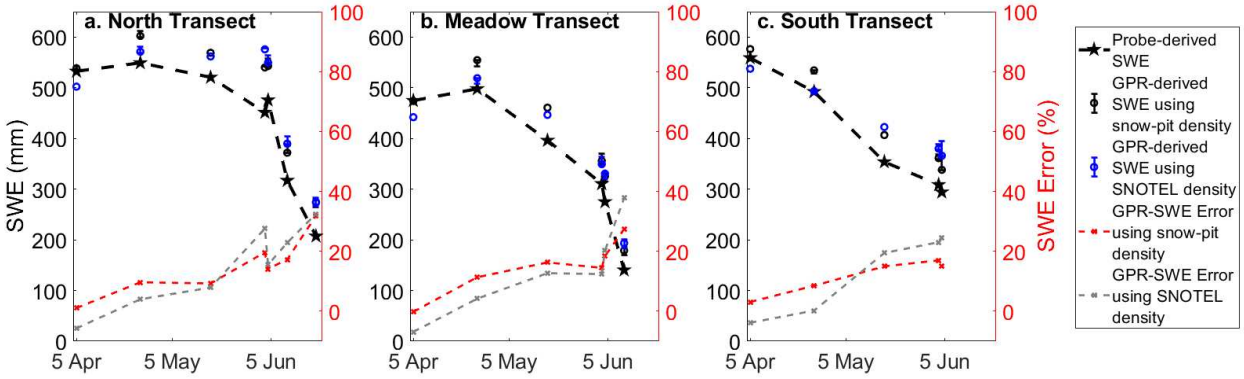

Figure 4.13: SWE calculations from probe and snowpit datasets compared to SWE calculations from GPR based on dry-snow density models. Percent error shown in red represents the GPR SWE calculations based on the density model from the local snowpit. Percent error shown in gray represents the GPR SWE calculations based on the density model from Joe Wright SNOTEL station. Percent error given as the mean percent error from the transect.

4.8 GPR Measurements of LWC using Terrestrial LiDAR Scans

TLS-derived distributed snow depth maps (Figure 4.14) contained depth distributions that differ significantly from the probed depth distribution and a significant number of the TLS-derived depths are negative. The 25 April distributed snow depth map has ~4% of depth values less than 0 m and ~65% of depth values between 0-1 m. The mean is 1.18 m with a standard deviation of 1.91 m. The 3 June distributed snow depth map has ~10% of depth values < 0 m and ~74% of depth values between 0 and 1 m. The mean is 0.87 m with a standard deviation of 1.86 m. For the 25 April survey, coincident *twt* was used with TLS-derived snow depths (Equation 3.7) to calculate LWC (Figure 4.15). TLS-derived snow depths outside of four standard deviations of the probed depths mean were used in the LWC calculations. The maximum probe-derived LWC observed on 25 April was ~5 vol. %. The morning Meadow Transect survey yielded a mean LWC value of 10 vol. %, with 80.0% of LWC calculations exceeding the maximum probe-derived LWC. The midday Meadow Transect survey yielded a mean LWC value of 9.5 vol. %, with 72.4% of LWC calculations exceeding the maximum probe-derived LWC. The morning South Transect survey yielded a mean LWC value of 12.1 vol. %, with 62.1% of LWC calculations exceeding the maximum probe-derived LWC. The midday South Transect survey yielded a mean LWC value of 12.7 vol. %, with 67.6% of LWC calculations exceeding the maximum probe-derived LWC. Given the distribution of TLS-derived snow depths and LWC calculations, their validity is questionable.

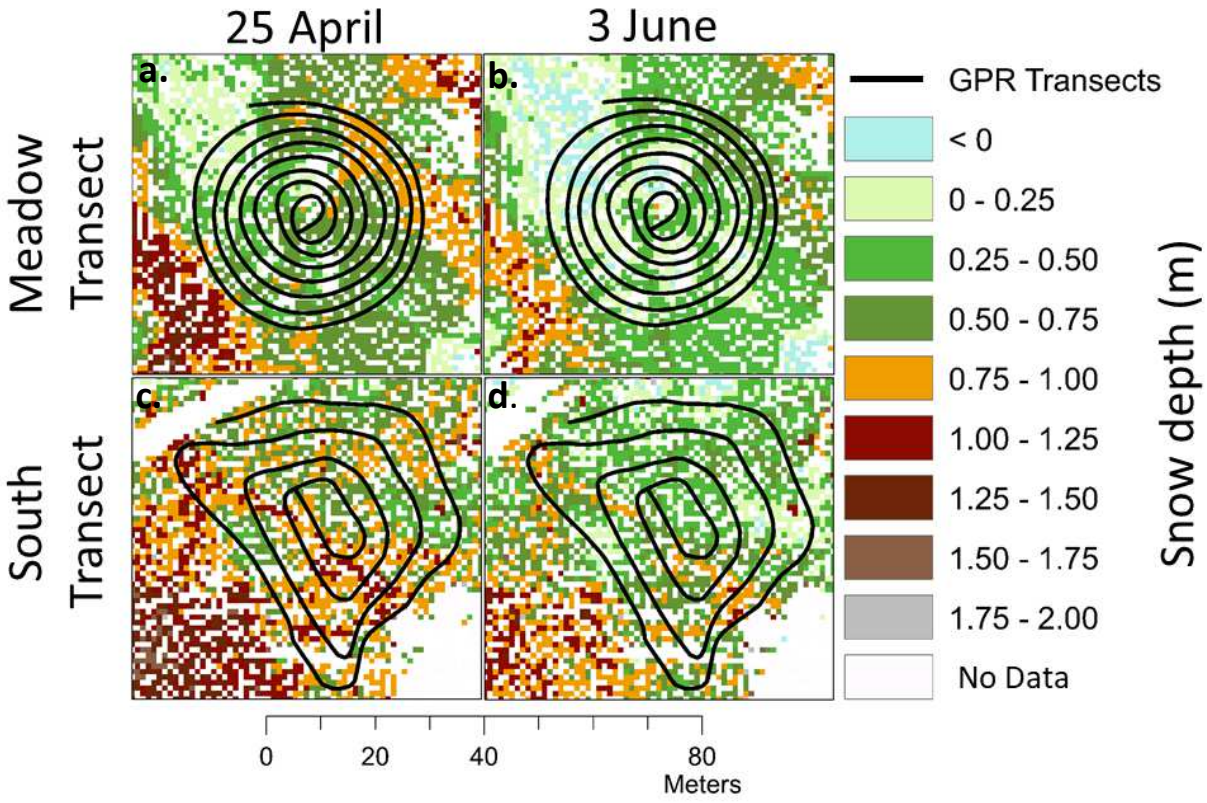

Figure 4.14: TLS-derived snow depths for the Meadow Transect on 25 April (a.) and 3 June (b.) and for the South Transect on 25 April (c.) and 3 June (d.). GPR tracks are overlain. Snow depths are gridded at 1 m resolution.

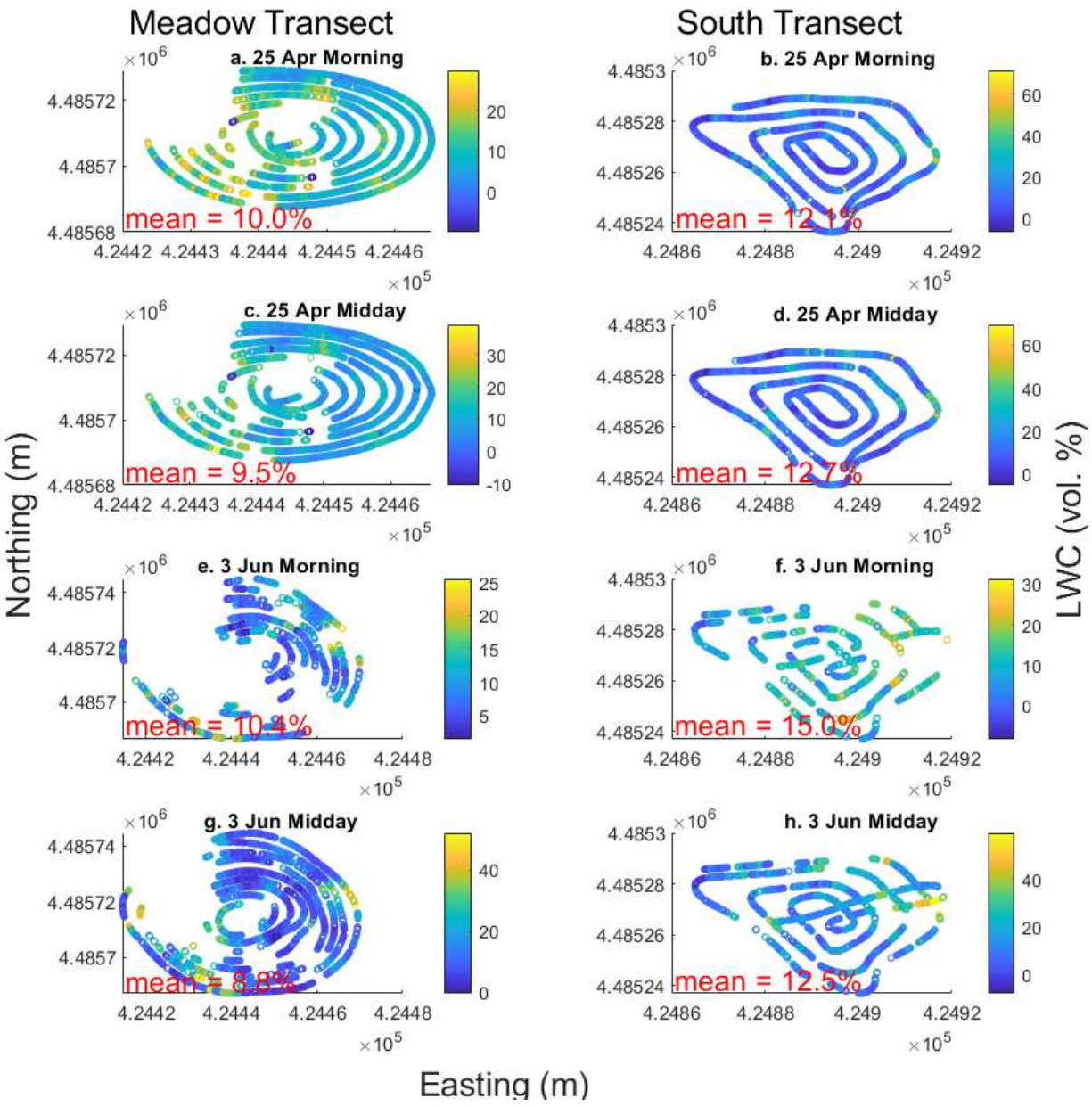

Figure 4.15: 25 April LWC measurements derived from GPR and TLS for morning surveys on the Meadow (a.) and South (b.) Transects and for midday surveys on the Meadow (c.) and South (d.) Transects. 3 June LWC measurements derived from GPR and TLS for morning surveys on the Meadow (e.) and South (f.) Transects and for midday surveys on the Meadow (g.) and South (h.) Transects. Snow depths outside of four standard deviations from the probed depths mean are removed from analysis, resulting in discontinuous LWC measurements.

The validity of TLS-derived snow depths was assessed through manual inspection of the point cloud for the snow-off TLS scan, examination of pictures and notes from UNAVCO, Inc. field engineers taken on the 29 August (Figure 4.16), and comparison of coincident probed depths and TLS-derived snow depths (Figure 4.17). Notes from the 29 August reveal that the

TLS was set-up in tall vegetation, up to 2 m in height, and pictures reveal the pervasiveness of the vegetation throughout the Meadow and South Transects. The snow-off TLS point cloud is surprisingly smooth and ground classification is inconsistent. In 2-D point cloud profiles, vegetation profiles are indiscernible, whereas vegetation profiles in the snow-on scans are clearly discernible in 2-D profile view. TLS-derived vegetation heights suggest a range of heights from 0-0.86 m, with a mean of 0.265 m. In a follow-up survey, 23 vegetation heights were manually measured along the Meadow Transect on 29 May 2020, which found a mean vegetation height of 0.39 m, a maximum of 1.20 m, and a minimum of 0.00 m. The follow-up vegetation survey was conducted within a week of snow melt-out on the Meadow Transect and provides a snapshot of this region before vegetation growth progresses. TLS-derived vegetation heights do not agree with vegetation heights noted on 29 August 2019, or the manually measured vegetation heights on 29 May 2020. It is likely that TLS penetration through the thick vegetation was limited. Negative TLS-derived snow depths (Figure 4.14) further support this notion, as the only contributors to elevation change on the Meadow and South Transects between 3 June and 29 August were snow disappearance and vegetation growth. Coincident TLS-derived snow depths and probed depths were limited for the 25 April Meadow (Figure 4.17a) and South (Figure 4.17b) Transects and the 3 June South Transect (Figure 4.17d). However, the majority (91 out of 135) of the probed depths on the 3 June Meadow Transect (Figure 4.17c) had coincident TLS-derived snow depths for comparison. The depth comparison appears to have a random distribution, with a mean disagreement of 0.44 m, a maximum disagreement of 0.831 m, and a minimum disagreement of < 0.01 m. Of the 120 coincident depths, the probed depths were greater than TLS-derived snow depths for 119 measurements. This provides further support for the possibility of limited TLS penetration in vegetation. Here, it is suggested that TLS

penetration through the vegetation present on 29 August was limited due to its oblique scan angle and the dense growth. Thus, LWC derived from the TLS datasets is considered unreliable for this analysis.

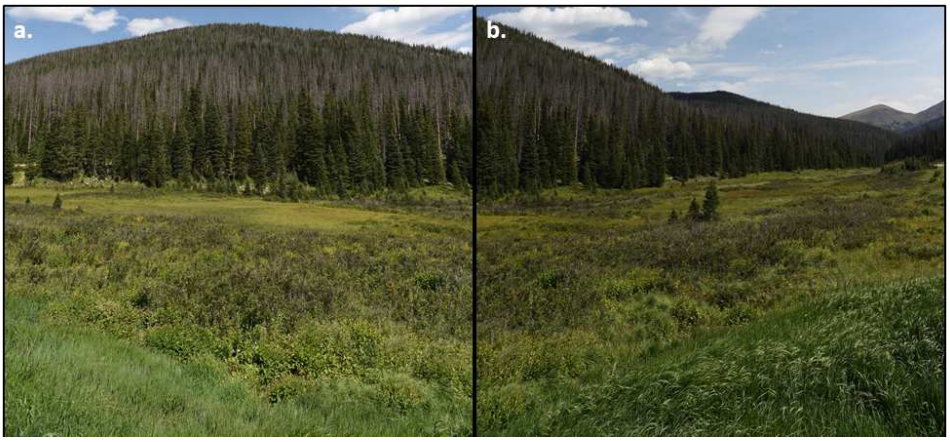

Figure 4.16: Pictures acquired on 29 August LiDAR survey on Meadow Transect looking east (a.) and looking south (b.). Vegetation was noted to be thick and as high as 2 m. Pictures courtesy of Keith Williams.

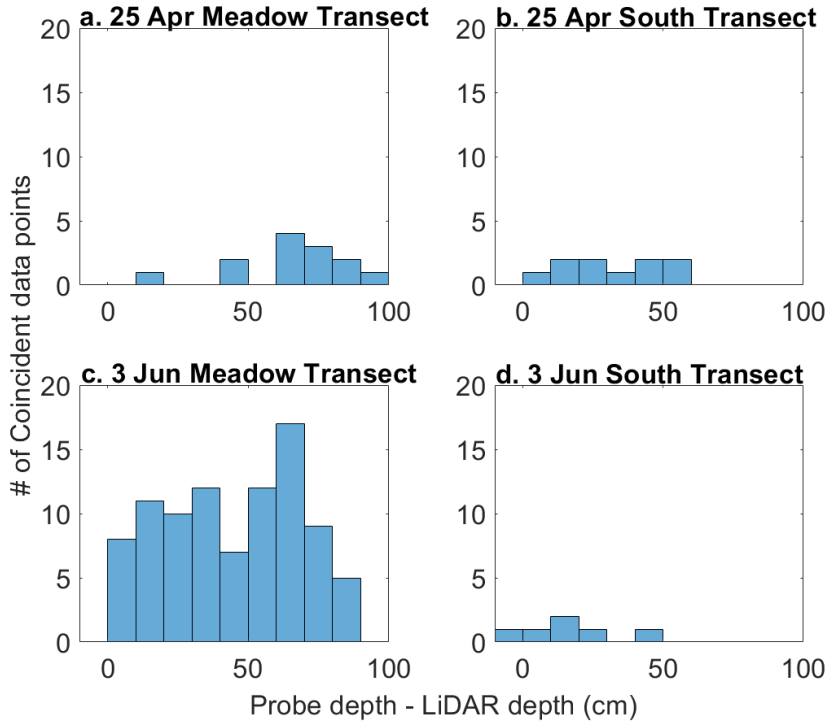

Figure 4.17: Histograms showing the difference between coincident probed depths and TLS-derived depths for the 25 April survey on the Meadow (a.) and South (b.) Transects and for the 3 June survey on the Meadow (c.) and South (b.) Transects.

5. Discussion

5.1 In-Situ Observations

In general, measured snow depths decrease throughout the melt season. In some cases, probed snow depths appear to increase between survey dates without any evidence of precipitation at Joe Wright SNOTEL station. This is highlighted by the 1.5 cm increase in median snow depth for the South Transect between 3 June and 4 June. Between these surveys, the snow depths for the North and Meadow Transects decreased by 5 cm and 4 cm, respectively, and the Joe Wright SNOTEL station recorded a 5 cm snow depth decrease. Discrepancies such as this are attributed to several possibilities: (1) probe methodological uncertainty, (2) spatial offset from previous survey's probed snow depth, and (3) GPS uncertainty. Depth probe uncertainty is ±0.05 m (Sturm and Holmgren, 2018) due to off-vertical probe penetration, presence of vegetation at the ground surface, and probe penetration into the snow-ground interface. The snow-ground interface was unfrozen and saturated throughout the study. Although efforts were taken to minimize over-probing, it is likely that this occurred, as evidenced by soil material on the probe tip. In the middle section of the Meadow Transect, the transect crosses a branch of the Michigan River multiple times. The stream profile, from the bank to the bed, is no wider than 6 m and the location of the probed point within this profile can influence the depth measurement substantially. Indeed, many of the depth anomalies occur in this region. Ideally, depth would always be measured in the same position. However, due to our method of using a handheld GPS unit to identify the transect and the 3 m probe-length to measure from one point to another, it is likely that very few snow depths were measured in identical locations over time. Furthermore, due to the interpolation process for probe geolocation, probes have an estimated

location error of ±0.25 m. The accuracy of the PPK solution for the Emlid RS+ is ±0.5 m, and contributes to the geolocation error. These three sources of uncertainty are believed to contribute to the development of anomalous snow depths from one survey date to the next.

Snowpit measured bulk snow density was consistently different between the three transects and showed different temporal trends: observed density was highest for the North Transect on 19 June, for the Meadow Transect on 3 June, and for the South Transect on 25 April (Figure 4.5a). For the Meadow and South Transects, density declined after the highest density was observed. As a note, the difference between the South Transect densities for 3 June and 4 June are within the wedge cutter uncertainty. One potential explanation for these trends are the development of preferential flowpaths. As the snowpack progresses through the melt season, preferential flowpaths can develop (Marsh and Woo, 1985), draining melt water to the ground-interface more efficiently as melt progresses (Techel and Pielmeier, 2011). Evidence for melt water flowpaths was observed in the 4 June and 10 June Meadow Transect snowpits, where piping crossed melt-freeze crusts. Melt is known to drive densification (Zwally and Jun, 2002; Rasmus, 2013), where the primary drivers are the sintering of snow grains, melt water percolation into snowpack pore spaces, and the refreezing of percolated water into ice lenses. However, the development of preferential flowpaths late in the melt season may work to decrease density in certain layers. Bulk snow density includes the masses of the frozen and liquid components of the snowpack (Equation 2.7) and saturation at the ground-snow interface can prevent drainage and increase LWC suspended in the snowpack, increasing density. However, flowpath development in the snowpack and at the ground-snow interface can effectively remove LWC, decreasing density. Thus, flowpath development may play a significant role in determining bulk snow density.

Snowpit LWC measurements taken by the SLF Snow Sensor varied from GPR LWC measurements taken ~1 m from the snowpit face by a mean of 78.7% and exhibited the same trend in LWC change for half of the surveys (Figure 4.5b). LWC trends are comparable between the SLF and GPR measurements for the Meadow Transect surveys on 25 April, 3 June, and 10 June, the South Transect survey on 4 June, and the North Transect survey on 25 April. Permittivity measurements taken by the SLF were converted to LWC using Equation 3.7, the same equation used to calculate LWC from GPR. Spatial variability may explain part of this discrepancy as LWC has been noted to change by up to 19.5 vol. % with 3 m distance (Webb et al., 2018a), but this is likely on one part of the explanation. As soon as the snowpit face is cut, water begins percolating out of the pore spaces and draining down the pit face; this is known as weeping (Techel and Pielmeier, 2011), and helps to explain the consistently higher SLF measurements earlier in the season. Differences between instrument method and the spatial footprint of those instruments likely contribute to the observed discrepancy. Two more common LWC measuring devices, the Denoth Meter (Denoth, 1994) and the Finnish Snow Fork (Sihvola and Tiurri, 1986), were compared and found to vary by a mean of 0.65 vol. % (Techel and Pielmeier, 2011). The Finnish Snow Fork measures LWC similarly to the GPR; it has two prongs and measures LWC through use of 1 GHz radio wave emission. The Denoth Meter is similar to the SLF Snow Sensor in that it is also a capacitance probe. The Denoth Meter and Finnish Snow Fork have similar footprints, which may explain their ability to measure LWC within such a tight constraint. The SLF Snow Sensor measures LWC over a volume of 72.7 cm^3, whereas the GPR measures LWC over a volume of ~$6.7x10^5$ cm^3, by emitting a pulse that travels through the snow in a cone defined by a Fresnel Radius that is sensitive to depth, permittivity, and frequency of the GPR (Leucci et al., 2003).

5.2 GPR Measurements of LWC

Several negative LWC values are calculated along the GPR transects, which is not physically realistic. Negative LWC measurements occur when the radar velocity calculated from probed snow depth and coincident *twt* is higher than the density-derived radar velocity. Since radar velocity is directly tied to permittivity, this permittivity imbalance is accommodated by negative LWC in Equation 3.7. Higher permittivity values result in slower radar velocities, so when permittivity, calculated from snow depth and *twt*, is too low, the equation compensates by outputting a negative LWC value. There are a number of potential causes for negative LWC, including probed snow depth over-estimates, removal of snow by the sled surface, or a poor comparison between the larger GPR footprint and much smaller probe footprint. All negative LWC values presented are between 0 and -1.0 vol. %, which are within the 1.5 vol. % uncertainty range given in Section 4.5 and are most likely related to snow depth over-estimates, as discussed in Section 3.9.1.

A central contribution of this research is understanding the physical drivers of LWC development. In this study, LWC values never exceeded 20 vol. % and, even in the latest part of the season, median LWC values did not exceed 7 vol. %. This finding agrees with LWC measured by continuously operating stations that found LWC values to rise as high as 10 vol. %, but only near the end of the melt season (Koch et al., 2014; Heilig et al., 2015; Schmid et al., 2015). Webb et al., (2018a) derived LWC at 3 m resolution along transects using GPR and TLS and found LWC values to be consistently higher on sloping transects than on flat-aspect transects. This disagrees with the findings presented here. The South Transect contained the most negative NI values (higher slopes, southerly aspect), yet was similar in LWC distribution to the Meadow Transect. The median South Transect LWC values were within 0.4 vol. % of median

Meadow Transect LWC values until 3 June, and the median LWC value for the South Transect on 4 June was 2.9 vol. % less than the median for the Meadow Transect. The South Transect had higher maximum LWC values for only 3 of its five survey dates (5 April, 3 June, and 4 June), with the Meadow Transect exhibiting higher maximum LWC values for the remaining dates (25 April and 17 May). The Meadow Transect parallels and crosses the Michigan River, and ground saturation may inhibit water drainage to the ground-snow interface as observed later in the season as ponds in the snowpits, whereas the South Transect has higher slopes that might provide more efficient output and drainage of melt water.

LWC values > 4.0 vol. % have been closely linked to melt water output (Schmid et al., 2015). This observation may help explain the negative trend for morning to midday ΔLWC observed on survey dates during the study period. As surface melt increases, water can no longer be held by capillary forces and drains through the snowpack (Schmid et al., 2015). Morning to midday ΔLWC and midday to evening ΔLWC median values are close to zero or negative for every survey date on the North Transect (Figures 4.6-4.8). The Meadow and South Transects exhibited mostly positive median ΔLWC for the morning to midday surveys, and negative median ΔLWC for the midday to evening surveys. The midday to evening ΔLWC result is expected, as received short-wave radiation decreases in the evening hours and there is typically less energy available to drive melt. However, the negative median ΔLWC values observed on the North Transect morning to midday surveys are puzzling, but be a result from the survey timing. Morning surveys on the North Transect were typically performed closer to 12:00 MDT and afternoon surveys experienced less flux in PDD than the Meadow or South Transects.

The highest LWC values for the North Transect were observed on 19 June, when standing water was observed at 0.05 m height at the base of the snowpit throughout the day. In

this case, the ground was saturated with water which prevented melt water output from the snowpack and saturated the base of the snowpack. The highest LWC values for the Meadow Transect were observed in the middle portion of the transect, coinciding with the Michigan River channel. Here, early-season streamflow likely saturated the base of the snowpack. Collectively, these observations suggest LWC very rarely exceeds 10 vol. %, and only in extreme cases, such as the end of the melt season, in close proximity to a stream, or where topographic lows and saturated ground prevent melt water drainage from the snowpack. However, given the extended length of the 2019 melt season at Cameron Pass and the lower than average air temperatures, it is possible that these observations would not hold in a more average snow year, with more intense melt water production over a shorter duration. LWC development exhibits year-to-year variability and is influenced by temperature trends and late-season storms (Heilig et al., 2015).

5.3 Objective 1: Controls on LWC Development

PDD is a temperature index model that is used to model melt in empirical relations (Hock 2003). Short-wave radiation is considered the primary driver for snow melt (DeWalle and Rango, 2008), but radiometers are not widespread and reanalysis products typically produce coarse (30 km spatial resolution) estimates (e.g., Climate Forecast System Reanalysis). Thus, the wide distribution of temperature sensors makes the PDD approach advantageous over energy balance models. The Joe Wright SNOTEL station is located ~1.4 km to the northeast of Cameron Pass and is ~30 m lower in elevation (using a 9.8°C/km lapse rate, temperatures should only differ by 0.3°C between Joe Wright SNOTEL station and Cameron Pass). As expected, PDD is correlated with daily observations of SWE-loss ($r^2 = 0.255$; Figure 4.2a) and discharge ($r^2 = 0.320$; Figure 4.2b). In the multi-variable linear regression for estimating ΔLWC (Figure 4.12), the ΔPDD coefficient is statistically significant at p-value < 0.05 and has the predicted sign

(positive) for all analyses except the 10 June individual survey date analysis. The NI x ΔPDD coefficient is statistically significant for 4 June (p-value < 0.05) and 10 June (p-value < 0.10), but the sign for the coefficients is positive, which was not predicted. NI is expected to modulate the available melt energy, such that regions with more negative NI contain higher ΔLWC. The 19 June survey is the only survey without a statistically significant ΔPDD coefficient, which is the survey with the least diversity in NI and LAI. The coefficients for ΔPDD and NI x ΔPDD are statistically significant (p-value < 0.05) for the ΔLWC dataset spanning the full time-series. Both coefficients are positive, and the NI x ΔPDD has a higher magnitude. The primary location for negative NI (i.e., sloped southerly aspect) is on the South Transect. Drainage at the ground-snow interface is hypothesized here to be more efficient on the South Transect than drainage on the North and Meadow Transects and LWC values are not too different between the Meadow and South Transects. Furthermore, evaporation of melt-water at the snow surface may contribute to lower ΔLWC on the South Transect due to higher exposure to short-wave radiation, though this seems unlikely due to decreased vapor pressure gradients during snow melt (Leydecker and Melack, 1999). In the range of NI studied in this dataset, it is possible that NI x ΔPDD is a better predictor for lower sloping environments, but further work documenting drainage at the ground-snow interface is required.

LAI < 1.0 and NI are expected to correlate negatively with LWC (DeWalle and Rango, 2008). In the single-variable linear regression, LAI (Figure 4.10) correlates negatively with LWC for 13 out of 17 surveys and NI correlates negatively with LWC for 10 out of 17 surveys. In the multi-variable linear regression for estimating ΔLWC, the coefficient sign varies for LAI and NI. The LAI coefficient is positive for the full dataset and all survey dates except the 4 June dataset. The NI coefficient is negative for the 4 June and 10 June surveys. Thus, LAI and NI are good

predictors of the distribution in LWC values, but modulate the available melt energy that drives ΔLWC. A factor that was not considered, but would certainly influence the NI and LWC relation, is hillslope drainage. Webb et al. (2018b) found that northern aspects develop more efficient flowpaths along the ground-snow interface than southern aspects. However, this study had limited variability in slope/aspect combinations to further evaluate this finding and more work is needed to better understand sub-snow drainage.

The multi-variable regression for estimating ΔLWC generated coefficients for several variables with statistical significance (p-value < 0.10) for the full dataset. These variables include LAI, NI, PDD, and NI x ΔPDD. The coefficients for LAI, ΔPDD, and NI x ΔPDD are positive, while the coefficient for NI is negative. The slope sign for LAI is unexpectedly positive, but may be compensated by the negative estimate for the LAI x ΔPDD coefficient (p-value >0.10), thereby representing a long-wave radiation input. The highest contributing variable is NI, with an appropriate slope sign. The next highest contributing variable is NI x ΔPDD. LAI x ΔPDD, regarded as a shading effect for canopy cover, was not statistically significant. Future work should calculate LAI at a higher spatial resolution and incorporate the solar zenith angle to better capture the variable shading in small meadows and higher long-wave input in denser forest areas.

In the multi-variable linear regression for estimating ΔLWC, the LAI x ΔPDD coefficient p-value is > 0.10 for the full dataset and all survey dates. Additionally, the LAI x NI coefficient p-value is > 0.10 for the full dataset and all survey dates except the 19 June survey (p-value < 0.05). These results suggest that LAI, NI, ΔPDD, and NI x ΔPDD are the most important ΔLWC variables considered in the analysis, but further work is needed to better distill their contributions to ΔLWC.

5.4 Objective 2: Radar SWE-retrieval Error Analysis

Density comparisons between manual observations and the Joe Wright SNOTEL station showed good agreement (mean difference = 6.03%; Figure 4.5) and were most similar to the North Transect densities. The Meadow Transect densities followed the Joe Wright SNOTEL station closely until 10 June, when it was 11% lower than the SNOTEL density. The South Transect densities were consistently different than the densities observed at the Joe Wright SNOTEL station (mean difference = 8.5%). Even though the Joe Wright SNOTEL station is not in the immediate vicinity of the study area, it is still relevant to the snowpack observed at Cameron Pass. Past analysis of the spatial variability exhibited around SNOTEL stations found that ~50% of SNOTEL stations exhibited depth measurements that were within 10% of the mean for the surrounding 1 km^2 (Meromy et al., 2013). The findings presented here suggest that SNOTEL measured densities may be useful for radar SWE-retrievals when no other density observation is available. Density tends to vary less than SWE or snow depth (Lopez-Moreno et al., 2013), but density variability with distance from SNOTEL station should be considered and a physical model (e.g., SNOWPACK) may improve these estimates. As it stands, density variability is a significant source of uncertainty in depth-based remote sensing SWE-retrievals (Rayleigh and Small, 2017).

During the melt season, radar SWE-retrievals were shown to overestimate SWE on all survey dates due to the presence of LWC in the snowpack (Figure 4.13). In general, error increased as the melt season progressed, and the snowpack had greater LWC values. This demonstrates that, in wet-snow, the use of a dry-snow density is insufficient to accurately map SWE in radar applications. The use of a dry-snow density to estimate SWE would add significant uncertainty to the identification of the peak SWE date, the progression of the melt season, and the monitoring of remaining SWE for water resources. In this analysis, the highest observed

SWE on the South Transect occurs on 5 April and for the North and Meadow Transects on 25 April (Joe Wright SNOTEL station peak SWE was observed on 18 April). The radar SWE-retrievals observe negligible SWE change between 25 April and 3 June on the North Transect, whereas true SWE decreased by 17.8%. The highest mean percent error is 37.8%, observed on the Meadow Transect on 10 June (using SNOTEL density). If a dry-snow density is used for radar-based SWE-retrievals, water managers could vastly overestimate remaining water resources.

5.5 GPR Measured LWC from TLS-derived Snow Depths

LWC measurements derived from TLS were shown to have significant uncertainty due to the impact of vegetation on determining the bare-earth elevation. TLS-derived snow depths are known to compare poorly with probe-derived snow depths in vegetated environments due to poor penetration through vegetation and a systematic misidentification of vegetation as ground-returns (Currier et al., 2019). This portion of the study would benefit significantly from a drone or airborne LiDAR scan (ALS), as the nadir scan angle results in better penetration through vegetation and produces more robust DTMs (Painter et al., 2016; Broxton et al., 2019; Currier et al., 2019). LiDAR used in snow remote sensing applications is limited by the availability of accurate DTMs. ICESat-2 is a satellite-borne LiDAR system whose primary objective is to detect elevation changes on the ice sheets (Markus et al., 2017). However, ICESat-2 also measures elevation changes for the rest of the world (90-day repeat coverage in the mid-latitudes), and SnowEx scientists are testing its applicability in mountain snowpacks. Unfortunately, high resolution DTMs are not widely available across the U.S.

The TLS results presented here highlight a major limitation in radar remote sensing: this method requires accurate snow depths and density to calculate LWC (Schmid et al., 2015; Webb

et al., 2018a). In radar applications, a nearby SNOTEL station may be available for a density measurement, but coincident snow depths will not be available to calculate LWC, thereby limiting the availability of appropriate radar velocities for measuring SWE. Bradford et al. (2009) developed a method of deriving LWC directly from GPR using an attenuation analysis, without the need for independent snow depths. However, this method requires GPR antennas that are suspended above the snow surface. This method shows promise in radar snow remote sensing, as permittivity could be directly calculated from the radargram and applied to accurately measure SWE. A similar method has been applied to GPS sensors in the L-1 frequency (1.58 GHz; Koch et al., 2014; Schmid et al., 2015). However, the attenuation LWC method has not been tested against the depth-derived LWC method and it may not be applicable for InSAR systems.

5.6 Future Directions

Polar and mountain regions are responding quickly to climate change and are warming at faster rates than low-elevation temperate and equatorial regions (Pepin et al., 2015; Huang et al., 2017). Despite technological advances in remote sensing, global SWE measurements remain difficult to obtain at sufficient spatial and temporal resolutions (Marshall et al., 2019). Real-time, high resolution SWE measurements are essential for the effective management of hydrologic resources. The NASA SnowEx mission is to develop an optimal space-borne approach for measuring SWE by testing several remote sensing instruments. The SnowEx 2020 Time Series Campaign tested the promising L-band (1-2 GHz) InSAR instrument (Deeb et al., 2011) with weekly repeat observations at 13 mountain sites scattered throughout the western U.S. (Marshall et al., 2019). Such test cases are essential, given the upcoming launch (2022) of the NASA-India L-band InSAR satellite, NISAR. Although SWE is not one of its science objectives, the

combination of radar frequency and repeat-orbit period provide a promising path forward, as coherence is more likely to be maintained. If these observations can be fully realized, it could provide global SWE estimates at 100 m resolution every 12 days.

Future work to support the testing of L-band radar SWE-retrievals in wet-snow should test radar signal-power attenuation methods (Bradford et al., 2009) and LWC modeling methods with a physical model (e.g., SNOWPACK; Bartelt and Lehning, 2002). If signal-power attenuation methods prove accurate and capable of directly measuring permittivity, this would provide the most accurate radar SWE-retrievals. Models have been shown to predict LWC accurately (Heilig et al., 2015) and could be applied in regions surrounding SNOTEL stations to interpolate density and model LWC, providing a wet-snow model for radar SWE-retrievals.

6. Conclusion

Although this study contributes to the understanding of LWC development, there are still many unknowns for the variability of LWC. The first objective of this study, to examine the contributing factors for LWC, was met by using LAI, NI, and PDD, as proxies for terrain, canopy cover, and available melt-energy. In the single-variable linear regressions, LAI had a negative relation with LWC for 13 of the 17 surveys and r^2 values were typically above 0.2, suggesting its viability for predicting LWC in forested regions. A higher resolution LAI product or different equation should be tested to find a better relation between LWC and LAI. NI had a negative relation with LWC for 10 of the 17 surveys, but r^2 values were typically less than 0.1. NI may have a more complex relation with LWC than previously thought, where higher may provide better output and drainage of melt water. Future studies should incorporate the effects of hillslope drainage as an LWC outlet, to better understand the spatiotemporal variability of LWC. In the multi-variable linear regression for the LWC dataset that spanned the full study period, LAI, NI, ΔPDD, and NI x ΔPDD had statistically significant (p-value < 0.10) coefficients for predicting ΔLWC. The r^2 for this regression was 0.182, which was expected given the scatter in the data. However, this result suggests that adequate models may accurately capture the spatial and temporal variability of LWC.

The high spatial variability of LWC results in highly variable snowpack permittivities that result in SWE overestimations when using radar-based SWE-retrievals. This was the subject of the second objective. Further understanding of the variability of LWC and snow density is required if L-band radar is to be a viable tool for snow remote sensing. Two possibilities for improving radar SWE-retrieval algorithms include signal attenuation analysis and physical

models. Signal attenuation analysis is dependent on frequency and could be applied to other SWE-sensing radar systems, such as SnowRadar (Yan et al., 2017a; 2017b). Studies have shown that physically based models can predict LWC at small plot scales, where the energy balance is well-known.

With the myriad of promising instruments, the future of snow remote sensing is bright. If proven viable, the global coverage of ICESat-2 would improve snow models around the world by providing a snapshot of snow depths in regions where snow is not studied. Ka-band InSAR techniques have been developed as a lower-cost alternative to LiDAR. Commercial, high-resolution satellite stereopairs are capable of producing snow depth maps in unforested regions. More recently, the C-band InSAR instrument on Sentinel-1 has proven capable of mapping the world's snow depth at 1 km resolution, which is promising, even if the physics of this method are poorly understood. Finally, should the SWE-measuring capabilities of L-band InSAR be fully realized, NISAR could provide 100 m resolution SWE-measurements globally, with or without clouds, every 12 days. Improvements in SWE-measuring capabilities will yield better water management practices and a stronger understanding of the changes occurring in the world's snow.

References

Barnett, T.P., J.C. Adam, and D.P. Lettenmaier (2005), Potential impacts of a warming climate on water availability in snow-dominated regions, *Nature*, 438, 303-309. https://doi.org/10.1038/nature04141

Bartelt, P. and M. Lehning (2002), A physical SNOWPACK model for the Swiss avalanche warning: Part I: numerical model, *Cold Regions Science and Technology*, 35(3), 123-145. https://doi.org/10.1016/S0165-232X(02)00074-5

Blindow, N. (2006), Ground Penetrating Radar, In: *Groundwater Geophysics*, Springer, Berlin.

Bradford, J.H., J.T. Harper, and J. Brown (2009), Complex dielectric permittivity measurements from ground-penetrating radar data to estimate snow liquid water content in the pendular regime, *Water Resources Research*, 45(8), 12 pp. https://doi.org/10.1029/2008WR007341

Brodzik, M.J., D.G. Long, M.A. Hardman (2018), Best Practices in Crafting the Calibrated, Enhanced-Resolution Passive-Microwave EASE-Grid 2.0 Brightness Temperature Earth System Data Record, *Remote Sensing*, 10(11), 1793. https://doi.org/10.3390/rs10111793

Broxton, P.D., W.J.D. van Leeuwen, and J.A. Biederman (2019), Improving Snow Water Equivalent Maps With Machine Learning of Snow Survey and Lidar Measurements, *Water Resources Research*, 55(5), 3739-3757. https://doi.org/10.1029/2018WR024146

Broxton, P.D., X. Zeng, and N. Dawson (2016), Why Do Global Reanalyses and Land Data Assimilation Products Underestimate Snow Water Equivalent?, *Journal of Hydrometeorology*, 17, 2743-2761. https://doi.org/10.1175/JHM-D-16-0056.1

Clow, D.W. (2010), Changes in the Timing of Snowmelt and Streamflow in Colorado: A Response to Recent Warming, *Journal of Climate*, 23, 2293-2306. https://doi.org/10.1175/2009JCLI2951.1

Currier, W.R., J. Pflug, G. Mazzotti, T. Jonas, J.S. Deems, K.J. Bormann, T.H. Painter, C.A. Hiemstra, A. Gelvin, Z. Uhlmann, L. Spaete, N.F. Glenn, and J.D. Lundquist (2019), Comparing Aerial Lidar Observations With Terrestrial Lidar and Snow-Probe Transects From NASA's 2017 SnowEx Campaign, *Water Resources Research*, 55(7), 6285-6294. https://doi.org/10.1029/2018WR024533

Daly, S.F., R. Davis, E. Ochs, and T. Pangburn (2000), An approach to spatially distributed snow modelling of the Sacramento and San Joaquin basins, California, *Hydrological Processes*, 14, 3257-3271.

Deeb, E.J., R.R. Forster, and D.L. Kane (2011), Monitoring snowpack evolution using interferometric synthetic aperture radar on the North Slope of Alaska, USA, *International Journal of Remote Sensing*, 32(14), 3985-4003. https://doi.org/10.1080/01431161003801351

Deems, J.S., T.H. Painter, and D.C. Finnegan (2013), Lidar measurement of snow depth: a review, *Journal of Glaciology*, 59(215), 467-479. https://doi.org/10.3189/2013JoG12J154

Denoth, A. (1994), An electronic device for long-term snow wetness recording, *Annals of Glaciology*, 19, 104-106. https://doi.org/10.3189/S0260305500011058

Dettinger, M.D., D.R. Cayan, M.K. Meyer, and A.E. Jeton (2004), Simulated hydrologic responses to climate variations and change in the Merced, Carson, and American River basins, Sierra Nevada, California, 1900-2099, *Climatic change*, 62, 283-317.

DeWalle, D.R. and A. Rango (2008), *Principles of Snow Hydrology*, Cambridge University Press, Cambridge, 410 pp.

Doesken, N., and A. Judson (1996), *The Snow Booklet: A Guide to the Science, Climatology, and Measurement of Snow in the United States,* Colorado State University, 86 pp.

Dozier, J., E.H. Bair, and R.E. Davis (2016), Estimating the spatial distribution of snow water equivalent in the world's mountains, *WIREs Water*, 3, 461-474. https://doi.org/10.002/wat2.1140

Dressler, K.A., S.R. Fassnacht, and R.C. Bales (2006), A Comparison of Snow Telemetry and Snow Course Measurements in the Colorado River Basin, *Journal of Hydrometeorology*, 7, 705-712. https://doi.org/10.1175/JHM506.1

Elder, K., J. Dozier, and J. Michaelsen (1991), Snow Accumulation and Distribution in an Alpine Watershed, *Water Resources Research*, 27(7), 1541-1552.

Fassnacht, S.R. and M. Hultstrand (2015), Snowpack variability and trends at long-term stations in northern Colorado, USA, *Proc IAHS*, 371, 131-136. https://doi.org/10.1007/s11707-018-0714-z

Fassnacht, S.R., K.S.J. Brown, E.J. Blumberg, J.I. Lopez-Moreno, T.P. Covino, M. Kappas, Y. Huang, V. Leone, and A.H. Kashipazha (2018), Distribution of snow depth variability, *Frontiers of Earth Science*, 12, 683-692.

Fierz, C., R.L. Armstrong, Y Durand, P. Etchevers, E. Greene, D.M. McClung, K. Nishimura, P.K Satyawali, and S.A. Sokratov (2009), *The International Classification for Seasonal Snow on the Ground*, IHP-VII Technical Documents in Hydrology, Paris.

Foster, J.L., A. Rango, D.K. Hall, A.T.C. Chang, L.J. Allison, and B.C. Diesen (1980), Snowpack monitoring in North America and Eurasia using passive microwave satellite data, *Remote Sensing of Environment*, 10, 285-298.

Gesch, D., M. Oimoen, S. Greenlee, C. Nelson, M. Steuck, and D. Tyler (2002), The National Elevation Dataset, *Photogrammetric Engineering and Remote Sensing, 68, 5-11.*

Goodison, B.E. and A.E. Walker (1993), Use of snow cover derived from satellite passive microwave data as an indicator of climate change, *Annals of Glaciology*, 17, 137-142. https://doi.org/10.3189/S0260305500012739

Gubler, H. and P. Weilenmann (1986), Seasonal Snow Cover Monitoring Using FMCW Radar, *International Snow Science Workshop*, 87-97.

Hall, D.K., C.J. Crawford, N.E. Digirolamo, G.A. Riggs, and J.L. Foster (2015), Detection of earlier snowmelt in the Wind River Range, Wyoming, using Landsat imagery, 1972-2013, *Remote Sensing of Environment*, 162, 45-54. https://doi.org/10.1016/j.rse.2015.01.032

Hammond, J.C., F.A. Saavedra, and S.K. Kampf (2018), Global snow zone maps and trends in snow persistence 2001-2016, *International Journal of Climatology*, 38, 4369-4383. https://doi.org/10.1002/joc.5674

Heilig, A., C. Mitterer, L. Schmid, N. Wever, J. Schweizer, H.P. Marshall, and O. Eisen (2015), Seasonal and diurnal cycles of liquid water in snow—Measurements and modeling, *Journal of Geophysical Research*, 120(10), 2139-2154. https://doi.org/10.1002/2015JF003593

Henn, B., T.H. Painter, K.J. Bormann, B. McGurk, A.L. Flint, L.E. Flint, V. White, and J.D. Lundquist (2018), High-Elevation Evapotranspiration Estimates During Drought: Using

Streamflow and NASA Airborne Snow Observatory SWE Observations to Close the Upper Tuolumne River Basin Water Balance, *Water Resources Research*, 54(2), 746-756. https://doi.org/10.1002/2017WR020473

Hock, R. (2003), Temperature index melt modelling in mountain areas, *Journal of Hydrology*, 282, 104-115. https://doi.org/10.1016/S0022-1694(03)00257-9

Hopkinson, C., M. Sitar, L. Chasmer, and P. Treitz (2004), Mapping Snowpack Depth beneath Forest Canopies Using Airborne Lidar, *Photogrammetric Engineering & Remote Sensing*, 8(3), 323-330. https://doi.org/10.14358/PERS.70.3.323

Huang, J., X. Zhang, Q. Zhang, Y. Lin, M. Hao, Y. Luo, et al. (2017), Recently amplified arctic warming has contributed to a continual global warming trend, *Nature Climate Change Letters*, 7, 875-880. https://doi.org/10.1038/s41558-017-0009-5

Kawashima, K., T. Endo, and Y. Takeuchi (1998), A portable calorimeter for measure liquid-water content of wet snow, *Annals of Glaciology*, 26, 103-106. https://doi.org/10.3189/1998AoG26-1-103-106

Keller, F., S. Goyette, and M. Beniston (2005), Sensitivity Analysis of Snow Cover to Climate Change Scenarios and Their Impact on Plant Habitats in Alpine Terrain, *Climatic Change*, 79, 299-319. https://doi.org/10.1007/s10584-005-5360-2

Kim, E. (2018), How can we find out how much snow is in the world?, *Eos*, 99. https://doi.org/10.1029/2018EO099939.

Klos, P.Z., T.E. Link, and J.T. Abatzoglou (2014), Extent of the rain-snow transition zone in the western U.S. under historic and projected climate, *Geophysical Research Letters*, 41, 4560-4568. https://doi.org/10.1002/2014GL060500

Koch, F., M. Prasch, L. Schmid, J. Schweizer, and W. Mauser (2014), Measuring Snow Liquid Water Content with Low-Cost GPS Receivers, *Sensors* 14, 20975-20999. https://doi.org/10.3390/s141120975

Koh, G., N.E. Yankielun, and A.I. Baptista (1996), Snow Cover Characterization Using Multiband FMCW Radars, *Hydrological Processes*, 10(12), 1609-1617.

Kwok, R. and G.F. Cunningham (2008), ICESat over Arctic sea ice: Estimation of snow depth and ice thickness, *Journal of Geophysical Research: Oceans*, 113, 17 pp. https://doi.org/10.1029/2008JC004753

Leucci, G., S. Negri, and M.T. Carrozzo (2003), Ground Penetrating Radar (GPR): an application for evaluating the state of maintenance of the building coating, *Annals of Geophysics*, 46(3), 481-489.

Leydecker, A. and J.M. Melack (1999), Evaporation from Snow in the Central Sierra Nevada of California, *Hydrology Research*, 30(2), 81-108. https://doi.org/10.2166/nh.1999.0005

Lievens, H., M. Demuzer, H.P. Marshall, R.H. Reichle, L. Brucker, I. Brangers, et al. (2019), Snow depth variability in the Northern Hemisphere mountains observed from space, *Nature Communications*, 10(4629). https://doi.org/10.1038/s41467-019-12566-y

Livneh, B. and A.M. Badger (2020), Drought less predictable under declining future snowpack, *Nature Climate Change*, 10, 452-458. https://doi.org/10.1038/s41558-020-0754-8

Logan, L. (1973) Basin-wide water equivalent estimation from snowpack depth measurements, *Role of Snow and Ice in Hydrology*, International Association of Hydrological Sciences, Wallingford, U.K., 864-884.

Lopez-Moreno, J.I., L. Leppanen, B. Luks, L. Holko, G. Picard, A. Sanmiguel-Vallelado, E. Alonso-Gonzalez, D.C. Finger, A.N. Arslan, K. Gillemot, A. Sensoy, A. Sorman, M.C.

Ertas, S.R. Fassnacht, C. Fierz, C. Marty (2020), Intercomparison of measurements of bulk snow density and water equivalent of snow cover with snow core samplers: Instrumental bias and variability induced by observers, *Hydrological Processes*.

Lopez-Moreno, J.I., S.R. Fassnacht, J.T. Heath, K.N. Musselman, J. Revuelto, J. Latron, E. Moran-Tejeda, and T. Jonas (2013), Small scale spatial variability of snow density and depth over complex alpine terrain: Implications for estimating snow water equivalent, *Advances in Water Resources*, 55, 40-52. https://doi.org/10.1016/j.advwatres.2012.08.010

Lundberg, A., C. Richardson-Naslund, and C. Andersson (2005), Snow density variations: consequences for ground-penetrating radar, *Hydrological Processes*, 20(7), 1483-1495. https://doi.org/10.1002/hyp.5944

Manickam, S. and A. Barros (2020), Parsing Synthetic Aperture Radar Measurements of Snow in Complex Terrain: Scaling Behaviour and Sensitivity to Snow Wetness and Landcover, *Remote Sensing*, 12(3), 31 pp. https://doi.org/10.3390/rs12030483

Markus, T. T. Neumann, A. Martino, W. Abdalati, K. Brunt, B. Csatho, S. Farrell, H. Fricker, A. Gardner, D. Harding, M. Jasinski, R. Kwok, L. Magruder, D. Lubin, S. Luthcke, J. Morison, R. Nelson, A. Neuenschwander, S. Palm, S. Popescu, C.K. Shum, B.E. Schutz, B. Smith, Y. Yang, and J. Zwally (2017), The Ice, Cloud, and land Elevation Satellite-2 (ICESat-2): Science Requirements, concept, and implementation, *Remote Sensing of Environment*, 190, 260-273. https://doi.org/10.1016/j.rse.2016.12.029

Marsh, P. and M.K. Woo (1985), Meltwater Movement in Natural heterogeneous Snow Covers, *Water Resources Research*, 21(11), 1710-1716.

Marshall, H.P., C. Vuyovich, C. Hiemstra, L. Brucker, K. Elder, J. Deems, et al. (2019), NASA SnowEx 2020 Experiment Plan (Science Plan).

Marshall, H.P. and G. Koh (2008), FMCW radars for snow research, *Cold Regions Science and Technology*, 52(2), 118-131. https://doi.org/10.1016/j.coldregions.2007.04.008

McCabe, G.J., M.P. Clark, and L.E. Hay (2007), Rain-on-Snow Events in the Western United States, *Bulletin of the American Meteorological Society*, 319-328. https://doi.org/10.1175/BAMS-88-3-319

McGrath, D., L. Sass, S. O'Neel, C. McNeil, S.G. Candela, E.H. Baker, and H.P. Marshall (2018), Interannual snow accumulation variability on glaciers derived from repeat, spatially extensive ground-penetrating radar surveys, *The Cryosphere*, 12, 3617-3633. https://doi.org/10.5194/tc-12-3617-2018

McGrath, D., R. Webb, D. Shean, R. Bonnell, H.P. Marshall, T.H. Painter, et al. (2019), Spatially Extensive Ground-Penetrating Radar Snow Depth Observations During NASA's 2017 SnowEx Campaign: Comparison with In Situ, Airborne, and Satellite Observations, *Water Resources Research*, 55, 10,026-10,036. https://doi.org/10.1029/2019WR024907

Meromy, L., N.P. Molotch, T.E. Link, S.R. Fassnacht, and R. Rice (2013), Subgrid variability of snow water equivalent at operational snow stations in the western US, *Hydrological Processes*, 27(17), 2383-2400. https://doi.org/10.1002hyp.9355

Moller, D., K.M. Andreadis, D.J. Bormann, S. Hensley, and T.H. Painter (2017), Mapping Snow Depth from Ka-Band Interferometry: Proof of Concept and Comparison with Scanning Lidar Retrievals, *IEEE Geoscience and Remote Sensing Letters*, 14(6), 886-890.

Molotch, N.P., M.T. Colee, R.C. Bales, and J. Dozier (2005), Estimating the spatial distribution of snow water equivalent in an alpine basin using binary regression tree models: the impact of digital elevation data and independent variable selection, *Hydrological Processes*, 19(7), 1459-1479. https://doi.org/10.1002/hyp.5586

Mote, P.W., S. Li, D.P. Lettenmaier, M. Xiao, and R. Engel (2018). Dramatic declines in snowpack in the western US, *Nature Partner Journals: Climate and Atmospheric Science*, 2. https://doi.org/10.1038/s41612-018-0012-1

Mote, T.L., A.J. Grundstein, D.J. Leathers, and D.A. Robinson (2003), A comparison of modeled, remotely sensed, and measured snow water equivalent in the northern Great Plains, *Water Resources Research*, 39(8).

Niittynen, P., R.K. Heikkinen, and M. Luoto (2018), Snow cover is a neglected driver of Arctic biodiversity loss, *Nature Climate Change*, 8, 997-1001. https://doi.org/10.1038/s41558-018-0311-x

Painter, T.H., D.F. Berisford, J.W. Boardman, K.J. Bormann, J.S. Deems, F. Gehrke, et al. (2016), The Airborne Snow Observatory: Fusion of scanning lidar, imaging spectrometer, and physically-based modeling for mapping snow water equivalent and snow albedo, *Remote Sensing of Environment*, 184, 139-152. https://doi.org/10.1016/j.rse.2016.06.018

Pepin, N., R.S. Bradley, H.F. Diaz, M. Baraer, E.B Caceres, N. Forsythe, et al. (2015), Elevation-dependent warming in mountain regions of the world, *Nature Climate Change Letters*, 5, 424-430. https://doi.org/10.1038/nclimate2563

Pomeroy, J.W., D.S. Bewley, R.L.H. Essery, N.R. Hedstrom, T. Link, R.J. Granger, J.E. Sicart, C.R. Ellis, and J.R. Janowicz (2006), Shrub tundra snowmelt, *Hydrological Processes*, 20(4), 923-941. https://doi.org/10.1002/hyp.6124

Proksch, M., N. Rutter, C. Fierz, and M. Schneebeli (2016), Intercomparison of snow density measurements: bias, precision, and vertical resolution, *The Cryosphere*, 10, 371-384. https://doi.org/10.5194/tc-10-371-2016

Raleigh, M.S. and E.E. Small (2017), Snowpack density modeling is the primary source of uncertainty when mapping basin-wide SWE with Lidar, *Geophysical Research Letters*, 44, 3700-3709. https://doi.org/10.1002/2016GL071999

Rasmus, S. (2013), Spatial and Temporal Variability of Snow Bulk Density and Seasonal Snow Densification Behavior in Finland, *Geophysica*, 49, 53-74.

Reach RS+ – RTK GPS receiver for high precision surveying, *Emlid*. Available from: https://emlid.com/reachrs/ (Accessed 23 June 2020).

Rial, F.I., H. Lorenzo, M. Pereira, and J. Armesto (2009), Analysis of the Emitted Wavelet of High-Resolution Bowtie GPR Antennas, *Sensors*, 9(6), 4230-4246. https://doi.org/10.3390/s90604230

Roth, K., R. Schulin, H. Fluhler, and W. Attinger (1990), Calibration of time domain reflectometry for water content measurement using a composite dielectric approach, *Water Resources Research*, 26(10), 2267-2273.

Ryan, W.A., N.J. Doesken, and S.R. Fassnacht (2008), Evaluation of Ultrasonic Snow Depth Sensors for U.S. Snow Measurements, *Journal of Atmospheric and Oceanic Technology*, 25(5), 667-684. https://doi.org/10.1175/2007JTECHA947.1

Saito, K., S. Ogawa, M. Aihara, and K. Otowa (2001), Estimates of LAI for Forest Managaement in Okutama, *22nd Asian Conference on Remote Sensing,* 5-9 November 2001.

Sandmeier, K.J. (2019), Reflexw – GPR and seismic processing software, *Sandmeier*. Available from: https://www.sandmeier-geo.de/reflexw.html (Accessed 23 June 2020).

Schmid, L., A. Heilig, C. Mitterer, J. Schweizer, H. Maurer, R. Okorn, and O. Eisen (2014), Continuous snowpack monitoring using upward-looking ground-penetrating radar technology, *Journal of Glaciology*, 60(221), 509-525. https://doi.org/10.3189/2014JoG13J084

Schmid, L., F. Koch, A. Heilig, M. Prasch, O. Eisen, W. Mauser, and J. Schweizer (2015), A novel sensor combination (upGPR-GPS) to continuously and nondestructively derive snow cover properties, *Geophysical Research Letters*, 42, 3397-3405. https://doi.org/10.1002/2015GL063732

Serreze, M.C., M.P. Clark, R.L. Armstrong, D.A. McGinnis, and R.S. Pulwarty (1999), Characteristics of the western United States snowpack from snowpack telemetry (SNOTEL) data, *Water Resources Research*, 35(7), 2145-2160. https://doi.org/10.1029/1999WR900090

Shean, D.E., O. Alexandrov, Z.M. Moratto, B.E. Smith, I.R. Joughin, C. Porter, and P. Morin (2016), An automated, open-source pipeline for mass production of digital elevation models (DEMs) from very-high resolution commercial stereo satellite imagery, *ISPRS Journal of Photogrammetry and Remote Sensing*, 116, 101-117. https://doi.org/10.1016/j.isprsjprs.2016.03.012

Shi, J. and J. Dozier (2000), Estimation of snow water equivalence using SIR-C/X-SAR. I. Inferring snow density and subsurface properties, *IEEE Transactions on Geoscience and Remote Sensing*, 38(6), 2465-2474.

Shi, J., C. Xiong, and L. Jiang (2016), Review of snow water equivalent microwave remote sensing*, Science China: Earth Sciences*, 4, 731-745. https://doi.org/10.1007/s11430-015-5225-0

Sicart, J.E. and R.L.H. Essery (2004), A Sensitivity Study of Daytime Net Radiation during Snowmelt to Forest Canopy and Atmospheric Conditions, *Journal of Hydrometeorology*, 5, 774-784.

Sihvola, A. and M. Tiuri (1986), Snow Fork for Field Determination of the Density and Wetness Profiles of a Snow Pack, *IEEE Transactions on Geoscience and Remote Sensing,* GE-24(5), 717-721.

SLF Snow Sensor – User Manual, *FPGA Company*. Available from: https://fpga-company.com/wp-content/uploads/2018/12/SLFSnowSensor-User-Manual-Version-1.4.pdf (Accessed 23 June 2020).

Snauffer, A.M., W.W. Hsieh, and A.J. Cannon (2016), Comparison of gridded snow water equivalent products with in situ measurements in British Columbia, Canada, *Journal of Hyrology*, 541, 714-726. https://doi.org/10.1016/j.jhydrol.2016.07.027

Snow Survey and Water Supply Forecasting Program, *National Water and Climate Center (USDA)*. Available from: https://www.wcc.nrcs.usda.gov/snotel/program_brochure.pdf (Accessed on 22 June 2020).

Stewart, I.T., D.R. Cayan, and M.D. Dettinger (2005), Changes toward Earlier Streamflow Timing across Western North America, *Journal of Climate*, 18, 1136-1155. https://doi.org/10.1175/JCLI3321.1

Sturm, M. and J. Holmgren (2018), An Automatic Snow Depth Probe for Field Validation Campaigns, *Water Resources Research*, 54, 9695-9701. https://doi.org/10.1029/2018WR023559

Takala, M., K. Luojus, J. Pulliainen, C. Derksen, J. Lemmetyinen, J.P. Karna, et al. (2011), Estimating northern hemisphere snow water equivalent for climate research through

assimilation of space-borne radiometer data and ground-based measurements, *Remote Sensing of Environment*, 115, 3517-3529.

Techel, F. and C. Pielmeier (2011), Point observations of liquid water content in wet snow – investigating methodical, spatial and temporal aspects, *The Cryosphere*, 5, 405-418. https://doi.org/10.5194/tc-5-405-2011

Tsai, Y.L.S., A. Dietz, N. Oppelt, and C. Kuenzer (2019), Remote Sensing of Snow Cover Using Spaceborne SAR: A Review, *Remote Sensing*, 11, 1456. https://doi.org/10.3390/rs11121456

Varhola, A., N.C. Coops, M. Weiler, and R.D. Moore (2010), Forest canopy effects on snow accumulation and ablation: An integrative review of empirical results, *Journal of Hydrology*, 392, 219-233.

Warren, S.G. (1982), Optical properties of snow, *Review of Geophysics*, 20(1), 67-89.

Webb, R.W., K.S. Jennings, M. Fend, and N.P. Molotch (2018a), Combining Ground-Penetrating Radar with Terrestrial LiDAR Scanning to Estimate the Spatial Distribution of Liquid Water Content in Seasonal Snowpacks, *Water Resources Research*, 54, 10,339-10,349. https://doi.org/10.1029/2018WR022680

Webb, R.W., S.R. Fassnacht, and M.N. Gooseff (2018b), Hydrologic flow path development varies by aspect during spring snowmelt in complex subalpine terrain, *The Cryosphere*, 12, 287-300. https://doi.org/10.5194/tc-12-287-2018

Wrzesien, M.L., M.T. Durand, T.M. Pavelsky, S.B. Kapnick, Y. Zhang, J. Guo, and C.K. Shum (2018), A New Estimate of North American Mountain Snow Accumulation From Regional Climate Model Simulations, *Geophysical Research Letters*, 45(3), 1423-1432. https://doi.org/10.1002/2017GL076664

Yan, J.B., D.G. Avestegui, J.W. McDaniel, Y. Li, F. Rodgriguez-Morales, J. Brozena, and C.J. Leuschen (2017a), Ultrawideband FMCW Radar for Airborne Measurements of Snow Over Sea Ice and Land, *IEEE Transactions on Geoscience and Remote Sensing*, **55**(2), 834-843.

Yan, J.B., S. Gogineni, F. Rodriguez-Morales, D. Gomez-Garcia, J. Paden, J. Li, et al. (2017b), Airborne Measurements of Snow Thickness Using ultrawide-band frequency-modulated-continuous-wave radar, *IEEE Geoscience and Remote Sensing Magazine*, **5**(2), 57-76.

Zwally, H.J. and L. Jun (2002), Seasonal and interannual variations of firn densification and ice-sheet surface elevation at the Greenland summit, *Journal of Glaciology*, 48(161), 199-207. https://doi.org/10.3189/172756502781831403